

# Probing Cosmology and Galaxy Cluster Structure with the Sunyaev–Zel’dovich Decrement vs. X–ray Temperature Scaling Relation

Cien Shang<sup>1</sup>, Zoltán Haiman<sup>2</sup>, Licia Verde<sup>3,4</sup>

<sup>1</sup>*Department of Physics, Columbia University, 550 West 120th Street, New York, NY 10027, USA; cien@phys.columbia.edu*

<sup>2</sup>*Department of Astronomy, Columbia University, 550 West 120th Street, New York, NY 10027, USA; zoltan@astro.columbia.edu*

<sup>3</sup>*Institute of Space Sciences (CSIC-IEEC), UAB, Barcelona 08193, Spain; verde@ieec.uab.es*

<sup>4</sup>*Department of Astrophysical Sciences, Princeton University, Ivy Lane, Princeton, USA*

20 November 2018

## ABSTRACT

Scaling relations among galaxy cluster observables, which will become available in large future samples of galaxy clusters, could be used to constrain not only cluster structure, but also cosmology. We study the utility of this approach, employing a physically motivated parametric model to describe cluster structure, and applying it to the expected relation between the Sunyaev–Zel’dovich decrement ( $S_\nu$ ) and the emission–weighted X–ray temperature ( $T_{\text{ew}}$ ). The slope and normalization of the entropy profile, the concentration of the dark matter potential, the pressure at the virial radius, and the level of non-thermal pressure support, as well as the mass and redshift–dependence of these quantities are described by free parameters. With a suitable choice of fiducial parameter values, the cluster model satisfies several existing observational constraints. We employ a Fisher matrix approach to estimate the joint errors on cosmological and cluster structure parameters from a measurement of  $S_\nu$  vs.  $T_{\text{ew}}$  in a future survey. We find that different cosmological parameters affect the scaling relation differently: predominantly through the baryon fraction ( $\Omega_m$  and  $\Omega_b$ ), the virial over–density ( $w_0$  and  $w_a$  for low- $z$  clusters) and the angular diameter distance ( $w_0$ ,  $w_a$  for high- $z$  clusters;  $\Omega_{DE}$  and  $h$ ). We find that the cosmology constraints from the scaling relation are comparable to those expected from the number counts ( $dN/dz$ ) of the same clusters. The scaling relation approach is relatively insensitive to selection effects and it offers a valuable consistency check; combining the information from the scaling relation and  $dN/dz$  is also useful to break parameter degeneracies and help disentangle cluster physics from cosmology. Our work suggests that scaling relations should be a useful component in extracting cosmological information from large future cluster surveys.

**Key words:** cosmological parameters – cosmology: theory – galaxies: clusters: general

## 1 INTRODUCTION

This work is motivated by large upcoming cluster surveys that utilize the Sunyaev–Zel’dovich (SZ) effect (Sunyaev & Zeldovich 1972) such as ACT<sup>1</sup>, APEX<sup>2</sup>, Planck<sup>3</sup>, and SPT<sup>4</sup>. As is well known, the SZ signal is nearly redshift independent, so these surveys are expected to be especially efficient in detecting high–redshift clusters. The expected catalogs will be sensitive probes of dark energy, and also useful in breaking degeneracies in local cluster surveys (for example,

the degeneracy between  $\sigma_8$  and  $\Omega_m$ ). The planned and on–going surveys will cover thousands of square degrees of sky, and detect on the order of  $\sim 10,000$  of clusters with masses over a few  $10^{14}M_\odot$ . For example, the SPT survey will cover 4,000 deg<sup>2</sup> of sky in 4 frequency channels (90, 150, 220, 270 GHz), and Planck aims to cover the whole sky in 9 frequency channels. These cluster samples will contain a significant amount of cosmological information.

Importantly, cosmological information can be extracted from large galaxy cluster catalogs in several complementary ways. For example, the cluster abundance is exponentially sensitive to the amplitude of matter density fluctuations, and the X–ray temperature function obtained from local cluster samples has been used to constrain  $\Omega_m$  and  $\sigma_8$  (e.g.,

<sup>1</sup> <http://www.physics.princeton.edu/act/>

<sup>2</sup> <http://bolo.berkeley.edu/apexsz/>

<sup>3</sup> <http://www.rssd.esa.int/index.php?project=Planck>

<sup>4</sup> <http://pole.uchicago.edu/>

Henry 2000, Ikebe et al. 2002). The redshift evolution of the abundance will be useful in constraining dark energy parameters, with statistical errors competitive with those in most other methods (e.g., Haiman et al. 2001; Albrecht et al. 2006). Small existing samples of tens of X-ray clusters out to  $z \sim 0.5$  already provide interesting constraints on the dark energy density  $\Omega_{DE}$  and equation of state parameter  $w$  (Henry 2004; Mantz et al. 2008; Vikhlinin et al. 2008). The cluster power spectrum also contains information on cosmology (Hu & Haiman 2003), both through the growth of fluctuations (Refregier et al. 2002) and through baryon acoustic features (Hu & Haiman 2003; Blake & Glazebrook 2003, Seo & Eisenstein 2003, Linder 2003). Combining the number counts and the power spectrum provides a cross-check and can allow a “self-calibration” to contain systematic errors in the mass-observable relation (Majumdar & Mohr 2004; Wang et al. 2004). In addition to the above, clusters could also be used as “standard rulers”. The measured gas fraction  $f_{\text{gas}}$ , which is derived from the observed X-ray temperature and density profiles, depends on the angular diameter distance as  $f_{\text{gas}} \propto D_A^{1.5}$  (e.g., Allen et al. 2008). To the extent that the gas fraction is predictable ab-initio from numerical simulations, this provides a measurement of  $D_A(z)$ . A complementary measurement of  $D_A(z)$  can be provided by combining SZ and X-ray signals, under the assumption that clusters are at least statistically spherical (e.g., Bonamente et al. 2006).

The gravitational potential of clusters is dominated by dark matter, whose behavior is determined by gravity alone, and is therefore robustly predictable (Navarro et al. 1997; hereafter NFW). If astrophysical processes in the gas were unimportant, the intracluster gas would evolve adiabatically, tracing the self-similar dark matter profile, and its global properties would obey simple scaling relations (e.g., Kaiser 1986). In fact, observed clusters indeed exhibit scaling relations that are tight, but which deviate significantly from the self-similar expectation. For example, the relation between X-ray flux ( $L_X$ ) and temperature ( $T_X$ ) is observed to be close to  $L_X \propto T_X^3$ , significantly steeper than the  $L_X \propto T_X^2$  power law expected in self-similar, adiabatic models. These observations could be explained by preferentially increasing the specific entropy of the cluster gas in low-mass clusters. Many variants of such models have been developed, based either on heat input from stars or nuclear black holes, or preferential elimination of the low-entropy gas by star-formation (see, e.g., a review by Voit 2005 and references therein). Our present study is motivated by the fact that in any such model, the predicted scaling relations will generically depend on the background cosmology. Using simple toy models, Verde et al (2002; hereafter VHS02) showed that the cosmological parameters indeed affect cluster scaling relations, i.e. relations among temperature, cluster size and SZ decrement. In small cluster samples (e.g., Morandi et al. 2007), the subtle cosmology-dependencies will be masked by the larger uncertainties in the physical modeling of cluster structure. However, given a sufficiently accurate measurement of the scaling relations, using thousands of clusters, it should become possible to place useful constraints simultaneously on cosmological parameters and the parameters of any given specific cluster physics model.

VHS02 argued that combining SZ and X-ray data will be particularly useful, because the SZ and X-ray signatures

depend on cosmological parameters differently, and singled out the relation between the Sunyaev-Zel’dovich decrement ( $S_V$ ) and the X-ray temperature ( $T_X$ ) as a promising probe of both cluster structure and cosmology. Afshordi (2008) showed that the measured relation between SZ decrement and angular half-light radius, which does not require X-ray data, may already help reduce the errors in cluster mass estimates. Younger et al. (2006) showed that combining number counts from SZ and X-ray surveys delivers constraints that are tighter than adding two independent measurements in quadrature; this synergy again arises because the SZ decrement and X-ray flux depend differently on the background cosmology. Finally, Aghanim et al. (2008) recently used hydrodynamical simulations, and studied how different values of the dark energy equation of state  $w$  affect SZ vs. X-ray scaling relations. They found relatively little direct sensitivity to  $w$  (which is consistent with our own findings; see discussion in § 3.1 below).

Despite the above few works, the utility of the scaling relations in probing cosmology remains relatively unexplored. We believe it deserves more investigation, for the following two reasons. First, data on the scaling relations will be automatically available (at least for a subset of clusters) once the planned SZ surveys are performed. Large catalogs of cluster temperatures (hundreds of clusters) already exist, and new, much deeper X-ray surveys are being proposed and planned, such as eROSITA and IXO<sup>5</sup>. Compared to the number counts, the scaling relation technique should be relatively less sensitive both to selection effects and to the relation between the observables and cluster mass. Second, as we will discuss below in detail, scaling relations derive cosmological information from a different combination of geometrical distances and non-linear growth than the other cluster observables. For this reason, they could not only be combined with other techniques to tighten constraints, but can also serve as useful consistency checks.

In this paper, we follow VHS02, and we focus on the relation between the total SZ flux decrement, encoded in integrated Compton  $y$  parameter, and the X-ray emission weighted temperature. There are other physical quantities, such as the X-ray luminosity or the central SZ decrement  $y_0$ . These quantities are especially sensitive to the properties of the cluster core, where cooling, star-formation, and feedback processes are most effective, and which is therefore the most difficult region of the cluster to model. The scatter in these quantities is known to be large, which will limit their utility for constraining cosmology. In contrast, the integrated Compton  $y$  parameter and the mean emission-weighted temperature show strong robustness to the above uncertainties (Reid & Spergel 2006 and Kravtsov, Vikhlinin & Nagai 2006 showed that similarly robust observables can be constructed from X-ray data, as well). An additional virtue of these two quantities is that they are relatively easy to measure, i.e. they do not require a detailed measurement of radial profiles.<sup>6</sup> The main improvements of the present study over the

<sup>5</sup> See <http://www.mpe.mpg.de/erosita/MDD-6.pdf> and <http://ixo.gsfc.nasa.gov>, respectively.

<sup>6</sup> We note, however, that the cluster core needs to be excised in cooling core clusters, in order not to affect the emission-weighted ICM temperature measurement. While it is possible to extract both the core temperature and the ICM temperature from a single

analysis of VHS02 are the following: (i) we include a full set of 8 cosmological parameters, representing the matter density  $\Omega_m$ , the dark energy density  $\Omega_{DE}$ , the baryon density  $\Omega_b$ , the Hubble constant  $h$  ( $h \equiv H/100\text{km s}^{-1}\text{Mpc}^{-1}$ ), two dark energy equation of state parameters  $w_0$  and  $w_a$  (see detailed definition in next section), the normalization of the matter density power spectrum  $\sigma_8$  and the “tilt” of the primordial power spectrum  $n_s$ . Note that we do not assume spatial flatness, so the 8 parameters are independent. VHS02 only included  $\Omega_m$ ,  $\sigma_8$  and  $h$  as free parameters. (ii) VHS02 adopted a simple spherical toy model for cluster structure, based on the virial theorem, to predict relations between different observable quantities. This approach has the virtue of simplicity, and makes it easier to interpret the results; however, such a simple cluster model is already in contradiction with existing data. Here we use a more elaborate, and more realistic phenomenological cluster model, with many free parameters. We explicitly require the model to satisfy existing observational constraints and we explore the impact of various cluster structure uncertainties on the final conclusions. (iii) We employ a Fisher matrix technique, instead of a Kolmogorov-Smirnov test as in VHS02. The Fisher matrix technique is a fast way of estimating joint parameter uncertainties in a multi-dimensional parameter space, and allows us to understand parameter degeneracies. (iv) Finally, we also study constraints from the number counts (including the effects of cluster structure uncertainty, mass-observable scatter and incompleteness), and we forecast the combined constraints from the scaling relations and the number counts.

The rest of this paper is organized as follows. In § 2, we describe the Fisher matrix technique and the physically motivated, phenomenological cluster model we adopt. The cluster model is compared against observations and simulations. We also explain our choice of fiducial values for cosmological parameters, cluster parameters and survey parameters. In § 3, we present our main results, i.e. the constraints on cosmological and cluster structure parameters. Proceeding pedagogically, we first include only the 8 cosmological parameters, then add increasing uncertainties from the cluster structure parameters to our analysis. We also explain in detail where the cosmological constraints from the scaling relations come from. In § 4, we compare the scaling relation technique with constraints from the number counts, and discuss various caveats and possible improvements to our results. We summarize our results and offer our conclusions in § 5.

## 2 CLUSTER MODEL AND FISHER MATRIX TECHNIQUE

### 2.1 Fisher matrix technique

We employ the Fisher matrix technique to forecast cosmological constraints from future surveys. The Fisher matrix is a quick way to estimate joint parameter uncertainties in a multi-parameter fit (Fisher 1935; Tegmark et al. 1997). It

is defined as,

$$F_{ij} = - \left\langle \frac{\partial^2 \ln \mathcal{L}}{\partial p_i \partial p_j} \right\rangle, \quad (1)$$

where  $\mathcal{L}$  is the likelihood for a certain observable, and  $p_i$  is the parameter set (including both cosmological and cluster structure parameters in our case). The best attainable covariance matrix  $C$  is simply the inverse of the Fisher matrix  $F$ ,

$$C_{ij} = (F^{-1})_{ij}, \quad (2)$$

and the constraint on any individual parameter  $p_i$ , marginalized over all other parameters, is  $\sqrt{(F^{-1})_{ii}}$ . Another advantage of the Fisher matrix technique is that it is easy to obtain joint constraints from several data sets or methods: the total Fisher matrix is just the sum of individual Fisher matrices as long as they are uncorrelated. In this paper, we assume that the different Fisher matrices are indeed independent; we justify this assumption in § 4.

The Fisher matrix approach makes the underlying assumption that the likelihood surface for the parameters is a multi-variate Gaussian. This is indeed the case if experimental errors are Gaussian-distributed and the model depends linearly on the parameters, but in general, this assumption does not hold, and is instead justified by invoking the central limit theorem in the presence of large number of independent data. The classical example is the CMB likelihood which is very close to Gaussian for the so-called “normal” or “physical” parameters (Kosowsky et al. 2002), but not necessarily for the standard cosmological parameters. However, for most cosmological models and future CMB data sets, especially if combined with external datasets or a weak prior on  $H_0$ , the CMB likelihood is very close to Gaussian even for the standard cosmological parameters (Komatsu et al. 2009). For degeneracies in parameters space that are described by non-linear parameter combinations, the Fisher matrix approach tends to underestimate the error-bars. Even with these limitations, the Fisher matrix approach is invaluable to estimate degeneracies among parameters and assess which data set combination can lift them.

### 2.2 Cluster model

Galaxy clusters are the largest gravitationally bound structures in the universe, and the properties of their dark matter halos should be relatively insensitive to astrophysical processes, which typically operate on scales much smaller than the size (i.e. virial radius) of a massive cluster. However, processes such as radiative cooling, star formation, heating and radiative feedback from active galactic nuclei, turbulence, and non-thermal pressure support from energetic particles accelerated in large-scale shocks, can all have significant impact on the thermal state and spatial distribution of gas in the intra-cluster medium (ICM), especially near the center of the cluster. Many aspects of the ICM remain poorly understood, despite extensive theoretical work, numerical simulations, and high-resolution observations.

There have been many approaches to building simplified models for cluster structure. Some are purely phenomenological formulae for the radial profiles, such as the simple 3-parameter “beta-model” (Cavaliere & Fusco-Femiano 1976), or the 17-parameter generalized NFW model proposed more

spectrum, this will inevitably introduce uncertainties, which will be discussed in § 4 below.

recently by Vikhlinin et al. (2006), which provides excellent fits to the range of observed X-ray profiles. Many studies have based the models on physical ingredients, generally assuming hydrostatic equilibrium, and parameterizing the processes listed above (see, e.g., Komatsu & Seljak 2001; Voit et al. 2002; Ostriker et al. 2005; Reid & Spergel 2006; Fang & Haiman 2008; Ascasibar & Diego 2008, and references therein).

In this paper, we do not attempt to build another *ab initio* physical cluster model. Instead, we use a “hybrid” phenomenological model, with physically motivated free parameters, similar to that proposed in Reid and Spergel (2006) and Fang and Haiman (2008). As we will show below, this model can satisfy most available observational constraints, and has the flexibility to include parameter variations. The ICM properties are assumed to be spherically symmetric, on average, and are determined by four factors: the radial entropy profile, the profile of the gravitational potential, the equations of hydrostatic equilibrium, and boundary conditions. Below, we describe how we incorporate these four factors into our cluster model.

*Entropy profile.* The radial entropy profile is parameterized by a power law,

$$K(x) \equiv \frac{T}{\rho^{\gamma-1}} = \hat{K} K_{\text{vir}} x^s, \quad (3)$$

where  $\rho$  and  $T$  are density and temperature of the ICM gas,  $\gamma$  is the adiabatic index, which we choose to be 5/3, appropriate for ideal monatomic gas, and  $x$  is the dimensionless radius, normalized by the virial radius  $R_{\text{vir}}$  of the cluster. The virial radius  $R_{\text{vir}}$  is defined to be the radius within which the mean density is equal to the virial density  $\rho_{\text{vir}}$  determined from numerical simulations (see equation 7 below).  $\hat{K}$  is the dimensionless entropy at the virial radius, and  $s$  quantifies the logarithmic slope of the entropy with radius. Note that convective stability requires the entropy  $K$  to be a monotonically increasing function of radius (Voit et al. 2002), so we require  $s \geq 0$ . The natural choice for the entropy scale is its value estimated using virial theorem,  $K_{\text{vir}} \equiv T_{\text{vir}} / (f_b \rho_{\text{vir}})^{\gamma-1}$ , where  $T_{\text{vir}} = GM_{\text{vir}} \mu m_p / (2R_{\text{vir}})$ . In above definitions,  $f_b$  is the baryon fraction of the universe ( $\Omega_b / \Omega_m$ ),  $m_p$  is the mass of a proton, and  $\mu$  is the mean molecular weight of the ICM (we adopt 0.59 as its value, appropriate for a fully ionized H-He plasma with helium mass fraction equal to 0.25). Note that  $K_{\text{vir}}$  is the characteristic entropy of a cluster in absence of non-gravitational forces rather than entropy at virial radius; in particular,  $\hat{K} > 1$  even without any feedback processes. Using the fitting formula given by Younger & Bryan (2007) and a slightly modified version of our current cluster model code, we estimate that  $\hat{K}$  is equal to 1.5 in the self-similar case.

*Dark matter halo gravitational potential.* We assume that the dark matter halos are spherically symmetric, and their density profiles are described by the NFW shape. The assumption of spherical symmetry can obviously be very inaccurate for individual clusters. We assume, however, that the main effect of the asymmetries is to introduce a scatter in the global scaling relations, rather than to change their mean (the accuracy of this assumption should be assessed in the future in three-dimensional simulations of a large sam-

ple of clusters). The NFW profile is expressed as

$$\rho_{\text{DM}}(r) = \frac{\delta_c \rho_c}{(r/r_s)(1+r/r_s)^2} \quad (4)$$

where  $r_s$  is the scale radius and  $\rho_c$  is the critical density of the universe. For a halo of DM mass  $M_{\text{DM}}$ , the two parameters  $\delta_c$  and  $r_s$  are determined from the concentration parameter  $c^{\text{NFW}}$  and the virial density  $\rho_{\text{vir}}$ ,

$$r_s = \frac{R_{\text{vir}}}{c^{\text{NFW}}} = \frac{1}{c^{\text{NFW}}} \left( \frac{3M_{\text{DM}}}{4\pi\rho_{\text{vir,DM}}} \right)^{1/3}, \quad (5)$$

$$\delta_c = \frac{\rho_{\text{vir,DM}}}{3\rho_c} \frac{(c^{\text{NFW}})^3}{\ln(1+c^{\text{NFW}}) - c^{\text{NFW}}/(1+c^{\text{NFW}})}. \quad (6)$$

Here  $\rho_{\text{vir,DM}} \equiv (\Omega_{\text{DM}}/\Omega_m)\rho_{\text{vir}}$ , with  $\Omega_{\text{DM}} \equiv (\Omega_m - \Omega_b)$ . We adopt a fitting formula from the numerical spherical collapse model calculation by Kuhlen et al. (2005) for  $\rho_{\text{vir}}$ ,

$$\rho_{\text{vir}} = 18\pi^2 \Omega_m(z) \rho_c(z) [1 + a\Theta^b(z)], \quad (7)$$

where  $\Theta(z) = \Omega_m^{-1} - 1$ ,  $a = 0.432 - 2.001(|w(z)|^{0.234} - 1)$ , and  $b = 0.929 - 0.222(|w(z)|^{0.727} - 1)$ , with  $w(z)$  the dark energy equation of state. Note that this formula differs slightly from other expressions for the virial overdensity that are commonly used in the literature (e.g., Bryan & Norman 1998), and it includes an explicit dependence on  $w$ . This feature is important to us, since we will constrain  $w$ , and, as we will find below, this dependence drives the constraints on  $w(z)$  at low redshift.

It is important to note that Equation (7) was obtained from spherical collapse calculations that assumed a constant  $w$ . In particular, one may wonder whether this fitting formula is still accurate when  $w$  is redshift dependent. To check the goodness of fit of Equation (7), we performed numerical calculations of the virial overdensity, using the spherical collapse model described by Kuhlen et al. We have found that Equation (7) is accurate to within 10% for time-varying  $w$  models in the range of  $-1.5 < w_0 < -0.5$ , and  $-|0.5w_0| < w_a < |0.5w_0|$ . More importantly, the virial density computed with the numerical method is systematically more sensitive to  $w_a$  than Equation (7) predicts. For example, we find that at redshifts  $z_{\text{collapse}} = 0.1, 0.2$ , and  $0.4$ , the fractional change in  $\rho_{\text{vir}}(z_{\text{collapse}})$ , when  $w_a$  is changed from  $w_a = 0$  to  $w_a = 0.21$  (i.e., by its  $1\sigma$  value; see below), and all other parameters are held fixed, is a factor of 3, 2, and 1.4 larger in the numerical calculation than predicted by the fitting formula. The higher sensitivity is easy to understand:  $\rho_{\text{vir}}$  at  $z_{\text{collapse}}$  depends on  $w(z > z_{\text{collapse}})$ , which at higher redshifts differs increasingly from the constant value  $w_0$ . We therefore conclude that using the Kuhlen et al. formula makes our constraints on  $w_a$  below conservative.

*Equations of hydrostatic equilibrium.* Below are the equations that we solve to obtain the cluster gas density and pressure profiles  $\rho_g(r)$ ,  $P(r)$ . The first is from the hydrostatic equilibrium condition, the second is from mass conservation,

$$\frac{dP(r)}{dr} = -\eta\rho_g(r) \frac{GM_{\text{tot}}(<r)}{r^2}, \quad (8)$$

$$\frac{dM_g(<r)}{dr} = 4\pi r^2 \rho_g(r), \quad (9)$$

where  $M_{\text{tot}}(<r)$  is the total mass within radius  $r$ , including both dark matter and baryons, and  $M_g(<r)$  is the total gas mass enclosed within radius  $r$ . The gas fraction  $f_g$ , which we

will use below, is defined to be  $M_g(< R_{\text{vir}})/M_{\text{tot}}(< R_{\text{vir}})$ . Finally, the parameter  $\eta \leq 1$  is introduced to allow for deviations from strict hydrostatic equilibrium. Physically, deviations from  $\eta = 1$  could represent any non-thermal pressure support (e.g., from cosmic rays and/or turbulence), and also lack of full virialization. In fact, allowing for turbulent support in the analytical model is known to be necessary in order to reproduce the density and temperature profiles for the ICM gas in simulations that include non-gravitational pre-heating (Younger & Bryan 2007).

*Boundary conditions.* The boundary condition at  $r = 0$  is specified by requiring that  $M_g(< r)$  is zero at the cluster center. The boundary condition at the virial radius is imposed by requiring that the gas pressure matches the momentum flux of the infalling gas,

$$P(R_{\text{vir}}) = \frac{\Omega_b}{3(\Omega_m - \Omega_b)} b \rho_{\text{DM}}(R_{\text{vir}}) v_{\text{ff}}^2 \quad (10)$$

where  $v_{\text{ff}}$  is the free-fall velocity from the turnaround radius. Assuming the turnaround radius is twice the virial radius, as in the spherical collapse model, we have  $v_{\text{ff}}^2 = GM_{\text{vir}}/R_{\text{vir}}$ . We follow Reid & Spergel (2006) and introduce a free parameter  $b$  to allow for an uncertainty in this condition.

The cluster model described above has 5 free parameters that capture uncertainties about cluster structure and evolution:  $K$ ,  $s$ ,  $c^{\text{NFW}}$ ,  $\eta$  and  $b$ . All of these quantities could additionally depend on both mass and redshift ( $\eta$  and  $s$  could also explicitly depend on radius, which, however, we ignore here). We use a power-law parameterization to allow for these dependencies,

$$p = p_{\text{norm}} \left( \frac{M}{M^*} \right)^{p_m} (1+z)^{p_z}, \quad (11)$$

where  $p$  could represent any of the 5 quantities. In equation 11, each function is described by 3 parameters, one for normalization, one for mass dependence and another for redshift dependence. We choose  $M^*$  to be  $10^{14} M_{\odot}$  (this choice is not essential, since changes to  $M^*$  can be compensated by changes in the normalization).

Several cautionary remarks about the above model are in order. First, the assumption of power-law mass and  $z$ -dependence is likely valid only when the variations over the observed mass and redshift range are small; the real dependence could be more complicated, especially if a wide mass or redshift range is considered. This could mean that actual data will not be fit adequately by such power-laws; in this case, additional parameters will likely have to be introduced (this possibility is addressed more quantitatively below).

Second, unlike Reid & Spergel (2006), we did not include additional modeling of the cluster cores. The reason for this is that core properties are known to vary significantly from cluster to cluster, and it is difficult to capture this variation with a universal parametrization. Fortunately, neglecting the core makes relatively little difference in our results. The two observables we focus on are temperature  $T$  and integrated Compton  $y$  parameter  $Y$ . We checked explicitly that introducing a flat entropy core within  $0.1 R_{\text{vir}}$  changes the value of  $Y$  by less than 2 percent (this result is consistent with Reid & Spergel 2006). When computing the emission-weighted temperature  $T$ , we excise the innermost regions (see eq. 17 below), which makes our temperature-observable similarly robust to core properties. This cut mimics the com-

mon procedures in existing observations, in which the ambient gas temperature is inferred either by excising the core region, or using a model (such as a cooling flow model) to eliminate the contribution from core regions. In order to minimize potential biases from the model-dependence of such cuts, we use a simple definition below.

Third, in reality, the cluster structure parameters will clearly have cluster-to-cluster variations: each of the parameters appearing in Equation (11) should therefore represent only a mean value. A scatter in any cluster structure parameter will induce a scatter in the value of the observables we predict. Below, we will derive constraints only from the mean observables (i.e. our signal is the mean  $Y - T$  scaling relation; the finite distribution of  $Y$  at fixed  $T$  is considered conservatively to be pure noise). An underlying scatter in a structure parameter can therefore have two effects on our results. First, the measurement error of the mean  $\langle Y \rangle$  is increased, which will correspondingly weaken our statistical constraints. Second, the mean inferred value of  $\langle Y \rangle$  can be biased, if the scatter in a parameter  $p_i$  introduces a skewed  $Y$ -distribution – and/or if the scatter is large, and it introduces Malmquist bias (i.e. the low- $Y$  tail of the clusters at fixed  $T$  could be preferentially missing from the sample). The first of these effect will be addressed below by allowing for a scatter in  $Y$  itself; the possible biases from the second effect are discussed in § 3.3.

In summary, our adopted baseline cluster model has  $5 \times 3$  parameters; given these parameters, we can numerically solve for the density and pressure profiles, and deduce all other ICM quantities. Below in § 2.5, we will use existing observational data and simulation results to determine the fiducial values of these parameters.

### 2.3 Fisher matrix for the scaling relation

Our first way of constraining cosmological parameters is to use the relation between the SZ flux  $S_{\nu}$  (measured through the integrated Compton  $y$  parameter,  $Y$ ) and the X-ray emission weighted temperature  $T_{\text{ew}}$ . The electrons in the hot ICM gas scatter the cosmic microwave background (CMB) photons, which distorts the CMB spectrum by the amount (e.g., Birkinshaw 1999; Carlstrom et al. 2002)

$$S_{\nu} = j_{\nu} Y, \quad (12)$$

where  $j_{\nu}$  is a known function of frequency,

$$j_{\nu}(x) = 2 \frac{(k_{\text{B}} T_{\text{CMB}})^3}{(hc)^2} \frac{x^4 e^x}{(e^x - 1)^2} \left[ \frac{x}{\tanh(x/2)} - 4 \right]. \quad (13)$$

Here  $x = h\nu/(k_{\text{B}} T_{\text{CMB}})$ ,  $T_{\text{CMB}}$  is CMB temperature,  $h$  is Planck constant,  $k_{\text{B}}$  is the Boltzmann constant, and  $c$  is the speed of light.  $j_{\nu}$  is positive at high frequency, negative at low frequency, and has a null at  $\nu \approx 220$  GHz. Physically, this means low-energy photons are Compton scattered by the hot electrons to higher energies, reducing the flux at low frequency and increasing it at high frequency.

The ICM properties are all encoded in  $Y$ . The total distortion within a fixed solid angle is given by

$$Y(\leq \theta) = 2\pi \int_0^{\theta} y(\theta') \theta' d\theta', \quad (14)$$

where  $y(\theta)$  is the Compton parameter along a given line of

sight,

$$y(\theta) = \frac{\sigma_T}{m_e c^2} \int P_e dl = \int \frac{\sigma_T n_e k_B T}{m_e c^2} dl, \quad (15)$$

and  $\sigma_T$  is the Thompson cross section. In this work, we use the value of  $Y$  integrated over the whole cluster, i.e. in equation (14) we set  $\theta = R_{\text{vir}}/D_A$ , with  $D_A$  the angular diameter distance. Combining equations (14) and (15), we get,

$$Y = \frac{\sigma_T k_B}{m_e c^2 D_A^2} \int n_e T dV_{\text{cluster}} \quad (16)$$

where  $V_{\text{cluster}}$  is the volume of cluster. Equation (16) clearly shows that the integrated SZ flux directly probes the thermal energy of ICM.

The emission-weighted temperature is calculated as

$$T_{\text{ew}} = \frac{\int_{0.15R_{500}}^{R_{500}} 4\pi r^2 dr \int d\nu \rho_g^2(r) \Lambda(\nu, T) T(r)}{\int_{0.15R_{500}}^{R_{500}} 4\pi r^2 dr \int d\nu \rho_g^2(r) \Lambda(\nu, T)} \quad (17)$$

where  $\Lambda(\nu, T)$  is the cooling function, calculated by a Raymond-Smith code (Raymond & Smith 1977) with metallicity  $Z = 0.3Z_\odot$ , and  $R_{500}$  is the radius with a mean enclosed overdensity of 500 relative to the critical density. Note that we do not integrate over the whole cluster – instead, we excise the inner region. This mimics the temperature measurements in X-ray observations, which either excise the cooling flow regions, or model and subtract their contribution. Since the inner radius ( $=0.15R_{500}$ ) has to be estimated from the data itself, this can introduce uncertainties or biases in the inferred  $T_{\text{ew}}$ . As we show in § 4 below, in order not to degrade the  $1\sigma$  constraints we obtain below, the inner radius has to be accurate (statistically) to within  $\approx 5\%$ , or the mass of the cluster to within  $\approx 15\%$ .

Given a  $Y(T)$  relation, we can construct the scaling-relation Fisher matrix for an individual cluster as

$$F_{ij}^{\text{sr, single}} = \frac{1}{\sigma_{Y,T}^2} \left. \frac{\partial Y}{\partial p_i} \right|_{T_{\text{ew}}} \left. \frac{\partial Y}{\partial p_j} \right|_{T_{\text{ew}}}, \quad (18)$$

where  $p_i$  and  $p_j$  are parameters to be constrained,  $\sigma_{Y,T}$  is the total statistical uncertainty on the value of  $Y$ , including both the intrinsic scatter  $\sigma_i$  in  $Y$  at fixed  $T$ , and the measurement uncertainty in  $Y$ ,  $\sigma_m$ ,  $\sigma_{Y,T}^2 = \sigma_i^2 + \sigma_m^2$ . Note that the partial derivative is taken at a fixed temperature, not at given cluster mass, since we are studying the relation of  $Y$  vs.  $T_{\text{ew}}$  not  $Y$  vs.  $M$ .

For a sample of clusters for which  $Y$  and  $T$  are both measured, the total Fisher matrix is the sum of the individual single-cluster Fisher matrices. We approximate this sum by an integration,

$$F_{ij}^{\text{sr, total}} = \Delta\Omega \int_{z_{\text{min}}}^{z_{\text{max}}} dz \frac{d^2V}{dzd\Omega} \int_{M_{\text{min}}(z)}^{\infty} dM \frac{dn}{dM}(M, z) F_{ij}^{\text{sr, single}} \quad (19)$$

where  $\Delta\Omega$ ,  $z_{\text{min}}$  and  $z_{\text{max}}$  are the solid angle, and the minimum and maximum redshifts covered by the survey,  $M_{\text{min}}(z)$  is the mass of smallest detectable cluster at each redshift,  $d^2V/dzd\Omega$  is the comoving volume element, and  $dn/dM(M, z)$  is the halo mass function. The form of this Fisher matrix is similar to the “follow-up” Fisher matrix used in Majumdar & Mohr (2003), except that their observable is the cluster mass itself (or a mass-like quantity), whereas our observable here is  $Y$ . We used the fitting formula by Jenkins et al. (2001) for the mass function (their

smoothed mass function, equation 9). In the fitting formula in Jenkins et al. (2001), the cluster mass  $M$  is defined to be the mass enclosed within a spherical region with overdensity of 180 with respect to the mean background matter density, whereas we defined clusters based on their virial overdensity with respect to the critical density (eq. 7 above). We used the NFW profile to convert the Jenkins et al. mass function to be consistent with our mass definition.

## 2.4 Fisher matrix for number counts

Another way of constraining cosmological parameters is through the cluster abundance. The observable in this case is the number of clusters in a given range of redshift and  $Y$ ,

$$N_{i\alpha} = \Delta\Omega \Delta z \frac{d^2V}{dzd\Omega}(z_i) \int_{M_{\text{min}}}^{\infty} g(Y_\alpha, M) \frac{dn(M, z_i)}{dM} dM \quad (20)$$

where  $M_{\text{min}}$  is a minimum mass we impose by hand (representing a sharp survey selection threshold; see discussion in § 3.3 below for allowing uncertainties in the selection), and  $g(Y_\alpha, M)$  is the probability that a cluster with mass  $M$  has a value of  $Y$  within the range of the  $\alpha$ th  $Y$ -bin. In this paper, for simplicity, we assume Gaussian scatter between  $M$  and  $Y$ , so that  $g(Y_\alpha, M)$  has an analytical form. Suppose bin  $Y_\alpha$  is specified by its minimum  $Y_{\text{min}}$  and maximum  $Y_{\text{max}}$ , and for a given mass  $M$ ,  $Y$  has a mean  $\bar{Y}(M)$  and r.m.s. of  $\sigma_{Y,M}$ . In this case,

$$\begin{aligned} g(Y_\alpha, M) &= \int_{Y_{\text{min}}}^{Y_{\text{max}}} \frac{1}{\sigma_{Y,M} \sqrt{2\pi}} \exp \left\{ -\frac{[Y - Y(M)]^2}{2\sigma_{Y,M}^2} \right\} dY \\ &= \frac{1}{2} \left\{ \text{erf} \left[ \frac{Y_{\text{max}} - Y(M)}{\sigma_{Y,M} \sqrt{2}} \right] - \text{erf} \left[ \frac{Y_{\text{min}} - Y(M)}{\sigma_{Y,M} \sqrt{2}} \right] \right\} \end{aligned} \quad (21)$$

Assuming Poisson errors dominate in the number counts ( $\sigma_N = \sqrt{N}$ ), and summing over all redshift- and  $Y$ -bins, the total Fisher matrix for the cluster abundance (Holder et al. 2001) is given by

$$F_{ij}^{\text{nc, total}} = \sum_{\alpha=1}^{N_z} \sum_{\beta=1}^{N_y} \frac{1}{N_{\alpha\beta}} \frac{\partial N_{\alpha\beta}}{\partial p_i} \frac{\partial N_{\alpha\beta}}{\partial p_j}, \quad (22)$$

where  $N_z$  and  $N_y$  are the number of redshift bins and  $Y$  bins, respectively. This expression ignores sample variance, whose effect on the cluster abundance constraints has been considered in detail in previous works (Hu & Kravtsov 2003; Lima & Hu 2004; Fang & Haiman 2006), and has been found to be modest, especially if the survey is sub-divided into many angular cells, and the variance is considered as signal, rather than noise; Lima & Hu (2004). Likewise, Holder et al. (2001) explored the validity of the Fisher matrix approach for forecasting cluster count constraints, and found it to be a good approximation, with the exception of the constraints for  $\sigma_8$ .

## 2.5 Fiducial parameter values

Here we summarize all the parameters in this work, and explain our choice of their fiducial values. Overall, the model parameters can be grouped into three categories: cosmological parameters, cluster model parameters and survey parameters.

*Cosmological parameters.* We include the following 8 standard cosmological parameters, with the 3-year results from the *Wilkinson Microwave Anisotropy Probe (WMAP)* experiment as their fiducial values (Spergel et al. 2007):  $\Omega_m = 0.244$ ,  $\Omega_{DE} = 0.756$ ,  $\Omega_b = 0.0413$ ,  $h = 0.72$ ,  $w_0 = -1$ ,  $w_a = 0$ ,  $\sigma_8 = 0.76$  and  $n_s = 0.96$ . Here  $w_0$  and  $w_a$  parametrize the dark energy equation of state,

$$w(z) = w_0 + w_a(1 - a) = w_0 + w_a \frac{z}{1+z}. \quad (23)$$

We do not assume a spatially flat universe, so the 8 cosmological parameters are independent. The more recent 5-year results from *WMAP* are consistent with the 3-year results.  $\sigma_8$  is slightly higher ( $\sigma_8 = 0.817$  from the combination of the *WMAP* result with baryon acoustic oscillations and supernovae; Dunkley et al. 2008). Adopting this new value would increase the number of detectable clusters, and tighten our constraints below. We emphasize that the number counts constrain all 8 parameters directly, while the scaling relation alone can only constrain 6 of them ( $\sigma_8$  and  $n_s$  do not affect scaling relation). Nevertheless, when combined with the number counts, the information from the scaling relation can indirectly help constrain  $\sigma_8$  and  $n_s$ , by breaking degeneracies, as we will demonstrate in § 3 below.

*Cluster model parameters.* The cluster model described in § 2.2 above has  $5 \times 3 = 15$  parameters, describing the normalization  $\hat{K}$  and logarithmic slope  $s$  of the gas entropy profile, the concentration  $c^{\text{NFW}}$  parameter for the dark matter halo profile, any contributions from non-thermal pressure  $\eta$ , and the gas pressure at the virial radius  $b$ , each with a normalization, redshift dependence and mass dependence. We set their fiducial values using results from simulations and observations.

The self-similar collapse model that invokes only gravity and shock heating predicts a universal entropy profile  $K(r) \propto r^{1.1}$  (Tozzi & Norman 2001; Borgani et al. 2001), which is in general agreement with observations outside the core (Ponman et al. 2003; Pratt et al. 2006). We therefore adopt this fiducial value for  $s$ , with no dependence on mass or redshift ( $s_m = s_z = 0$ ,  $s_{\text{norm}} = 1.1$ ).

The difference in the cluster mass inferred from weak lensing and X-ray measurements suggests that non-thermal pressure contributes about 10% to total gas pressure (Zhang et al. 2008), similar amounts have also been seen in simulations (Rasia et al. 2004; Kay et al. 2004; Faltenbacher et al. 2005), thus we adopt  $\eta = 0.9$  with no mass and redshift dependence.

For the concentration parameter  $c^{\text{NFW}}$ , we adopt the fiducial value that is directly computed from cosmological simulations in Voit et al. (2003),

$$c^{\text{NFW}}(M, z) = 8.5 \left( \frac{M}{10^{15} h^{-1} M_\odot} \right)^{-0.086} (1+z)^{-0.65}. \quad (24)$$

Note that unlike our other model parameters, in principle,  $c^{\text{NFW}}$  can be accurately computed ab-initio, using three-dimensional N-body or hydro simulations. However, the uncertainties are still significant, and the current results are in tension with X-ray observations (e.g., Duffy et al. 2008); for completeness, we therefore include it as a free parameter in our baseline model. Below, we will investigate the benefits of placing tight priors on this parameter (and we find the benefits to be small). For simplicity, we set  $b = 1$ ,

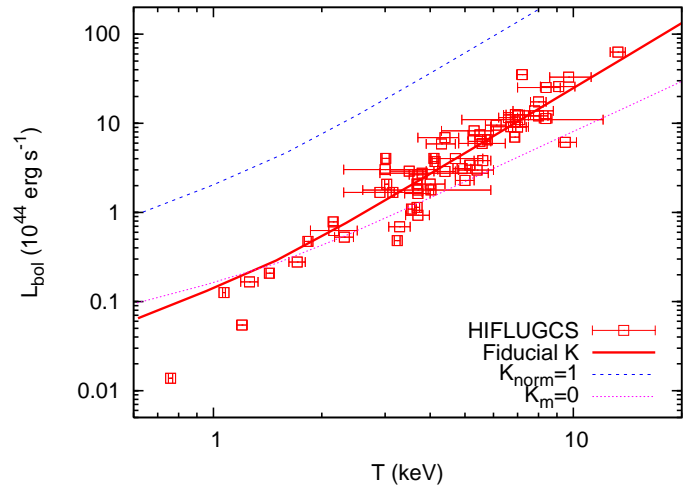


**Figure 1.** The  $L - T$  relation observed at low redshift, together with the predictions in our cluster model. The data points are from the HIFLUGCS cluster sample, with average redshift  $z = 0.05$  (Reiprich & Böhringer 2002). The thick solid [red] curve shows the  $L - T$  relation at this redshift, predicted in our fiducial cluster model with  $\hat{K}_{\text{norm}} = 2.4$ ,  $\hat{K}_m = -0.12$  and  $\hat{K}_z = 0.0$ . For comparison, we also show  $L - T$  curve for  $\hat{K}_{\text{norm}} = 1$  (dashed [blue] curve,  $\hat{K}_m$  and  $\hat{K}_z$  are kept at their fiducial values) and for  $\hat{K}_m = 0.0$  (dotted [thin red] curve,  $\hat{K}_{\text{norm}}$  and  $\hat{K}_z$  are kept at their fiducial values). Decreasing  $\hat{K}_{\text{norm}}$  increases the luminosity at a given temperature, whereas changing  $\hat{K}_m$  changes the slope.

which corresponds to the condition that all kinetic energy is transformed into thermal energy at the virial radius. Molnar et al. (2008) recently studied in detail the morphology and properties of virial shocks around galaxy clusters in smooth particle hydrodynamics (SPH) and adaptive mesh refinement (AMR) simulations of a sample of individual clusters. Although virial shocks are often preceded by external shocks farther out, closer to  $2 - 3R_{\text{vir}}$ , a significant fraction of the clusters' surface area is covered by strong virial shocks located at  $\sim R_{\text{vir}}$ , for which  $b = 1$  should be a good approximation. While detailed simulations could help refine the best fiducial choice for the mean boundary pressure, we do not expect the choice of this fiducial value to have a significant impact on our forecasts.

The fiducial value of  $\hat{K}$  is fixed by fitting the  $L - T$  relation. In Figure 1, we compare the observed  $L - T$  relation to the predicted values for the best-fit  $\hat{K}$ . The data points are from the HIFLUGCS cluster sample (Reiprich & Böhringer 2002). The bolometric luminosity is computed from

$$L = \int dV \int dv n_e(r) n_H(r) \Lambda(T, \nu), \quad (25)$$

where  $n_e$  and  $n_H$  are electron and proton number densities, respectively, and we assume a helium mass fraction of 25%. Unlike  $Y$ ,  $L$  is sensitive to the core properties, and the HIFLUGCS sample includes both cooling-core and non-cooling-core clusters. To account for this mixing, we modify the entropy profile in our model clusters, and add a flat entropy core of size  $0.1R_{\text{vir}}$ . The best-fit value of  $\hat{K}$  is found, by minimizing  $\chi^2$  using the data from Reiprich & Böhringer, to be  $2.4(M/M^*)^{-0.12}(1+z)^0$ .

This is in accordance with previous results on cluster formation and evolution. In particular, we find that the en-

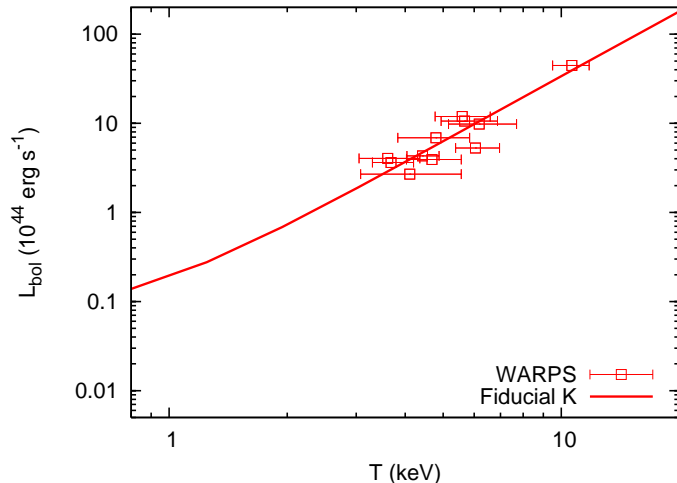


**Figure 2.** The  $L - T$  relation observed at high redshift ( $z \approx 0.8$ ), and predictions in our cluster model. The data-points are from the high-redshift WARPS clusters with average redshift  $\langle z \rangle = 0.8$ . The thick solid [red] curve is the prediction in our fiducial cluster model with  $\hat{K}_{\text{norm}} = 2.4$ ,  $\hat{K}_m = -0.12$  and  $\hat{K}_z = 0.0$ .

entropy is elevated ( $\hat{K}_{\text{norm}} > 1.5$ ), as expected by feedback processes, and also that the increase in entropy is more significant for lower-mass clusters, breaking the self-similar relation. For comparison, in the same figure we also plot the  $L - T$  curves expected for  $\hat{K}_{\text{norm}} = 1.0$  (dashed line,  $\hat{K}_m$  and  $\hat{K}_z$  are kept at their fiducial values) and  $\hat{K}_m = 0$  (dotted line,  $\hat{K}_{\text{norm}}$  and  $\hat{K}_z$  are kept at their fiducial values). Lowering  $\hat{K}_{\text{norm}}$  raises  $L$  at a given temperature, while lowering  $\hat{K}_m$  increases the slope.

We emphasize that  $\hat{K} = 1$ , as mentioned above, does not correspond to the gravitational-heating only case, and that, in agreement with previous results, the most massive clusters in Figure 1 fall on the observed  $L - T$  relation even without any non-gravitational heating. To verify this, we followed Fang & Haiman (2008), and used the fitting formula given in Younger & Bryan (2007) to compute the maximum entropy in the gravitational-heating only case. This entropy is found to be  $\approx 1.5K_{\text{vir}}$  at the virial radius. With our adopted set of cosmological parameters, a 10keV cluster has mass of  $3 \times 10^{15} M_{\odot}$ , and  $\hat{K} = 1.6$ ; the difference between our fiducial  $K$  and that of the simulation is only 0.1 around  $T = 10$  keV (this difference is due to the fact that our fiducial entropy profile is steeper than found in adiabatic simulations).

Though a successful fit in general, at the lowest temperatures shown in Figure 2 ( $T \lesssim 1\text{keV}$ ), the best-fit  $L - T$  relation has a slope that flattens slightly, in contrast with observations that indicate a steepening at these temperatures (e.g., Helsdon & Ponman 2000). This shows that our particular power-law parameterization (eq. 11) is insufficient in capturing the increase in the mean entropy at low temperatures. Correcting this deficiency would be possible by using different parameterizations (e.g., parameterizations that preferentially affect the cores of low-temperature clusters, such as the “entropy-floor” models; e.g., Fang & Haiman 2008). However, in this paper, we focus on clusters detectable in SZ experiments. These have a mass  $\gtrsim 10^{14} h^{-1} M_{\odot}$  (or equivalently, a mean temperature of

$T \gtrsim 1.5\text{keV}$ ), and the power-law models provide a good fit the  $L - T$  relation of these clusters (Fig. 2).

We also note that we do not find a need for  $\hat{K}$ , as expressed in the form of equation (11), to evolve with redshift. In Figure 2, we show the  $L - T$  relation predicted in our model, assuming  $\hat{K}_z = 0$ , at redshift  $z = 0.8$ , together with data from the high-redshift cluster sample from the Wide Angle ROSAT Pointed Survey (WARPS; with average redshift of  $\langle z \rangle = 0.8$ ). As the figure shows, the model provides an excellent match to the data. Although not immediately obvious, this conclusion is qualitatively in agreement with the result in Fang & Haiman (2008), who found that that if a fixed entropy floor is assumed to exist in all cluster at a given redshift, then this floor value has to decrease toward higher redshifts. The entropy floor is the difference between total entropy and baseline value (without non-gravitational heating). Our result indicates that the ratio of total entropy to baseline entropy is the same for low and high redshifts. This means that the difference is smaller for high-redshift clusters, since they have a higher density and a smaller baseline entropy. (For more details on this apparent coincidence, see Figure 6 and the related discussion in Fang & Haiman 2008).

Our parameterization allows us to vary the slope of the entropy profile  $s$ , which is necessary to fit temperature profiles measured in X-ray observations. This, in fact, is the main advantage of our parameterization compared to similar models that include a constant entropy floor, since the latter approach generically fails to match radial profiles (e.g., Younger & Bryan 2007 and references therein). In Figure 3, we show the temperature profile in our fiducial cluster model with  $s = 1.1$ , compared to the mean profile recently inferred from XMM-Newton observations (Leccardi & Molendi 2008). In this plot, we adopt  $z = 0.2$ , which is approximately the median redshift of the XMM-Newton cluster sample, and  $M = 10^{15} M_{\odot}$ , which corresponds to a mean temperature about 6 keV, approximately the temperature of a typical cluster in the sample. We follow Leccardi & Molendi (2008) to compute  $R_{180}$  as

$$R_{180} = 1780 \left( \frac{T}{5\text{keV}} \right)^{1/2} h(z)^{-1} \text{kpc}. \quad (26)$$

As shown in Figure 3, the model temperature profile is in good agreement with observations out to the radius of  $0.6R_{180}$  where data is available.

Finally, we compare the  $Y - M$  relation in our fiducial model with predictions from simulations. More specifically, in Figure 4, we show the  $Y_{200} D_A^2 - M_{200}$  relation in our fiducial model, together with the predictions for the same quantity in Nagai (2006) and Sehgal et al. (2007), who respectively use high-resolution hydrodynamical simulations, and N-body simulations of dark matter halos and a prescription for the corresponding gas distribution. Here  $Y_{200}$  and  $M_{200}$  are the SZ Compton  $y$  parameter and the total mass within the radius  $R_{200}$ . We note that Sehgal et al. integrate over a cylindrical region extending to an angular radius corresponding to  $R_{200}$ , while Nagai integrates over a sphere of radius  $R_{200}$ . For a fair comparison, we compute  $Y_{200}$  both ways. The upper solid [red] curve in Figure 4 is  $Y_{200}$  in a cylindrical region, while the lower solid [red] curve is that in a sphere. The redshift is set to be  $z = 0$ , to match Nagai’s simulation. We use the fitting parameters in row 2 of Table

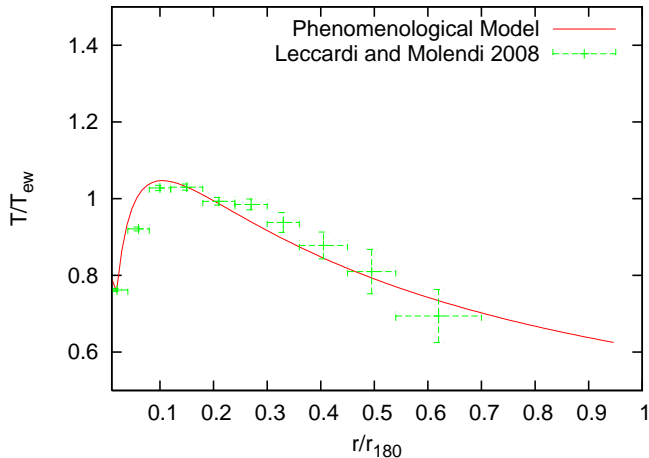


**Figure 3.** Radial temperature profile in our fiducial phenomenological model, in which the entropy profile has a logarithmic slope of  $s = 1.1$ , compared to recent XMM-Newton measurements of Leccardi & Molendi (2008). We adopt a redshift of  $z = 0.2$ , approximately the median redshift of the observed cluster sample, and a mass of  $M = 10^{15} M_{\odot}$ , which corresponds to a temperature of approximately 6 keV, close to the temperature of a typical cluster in the sample.

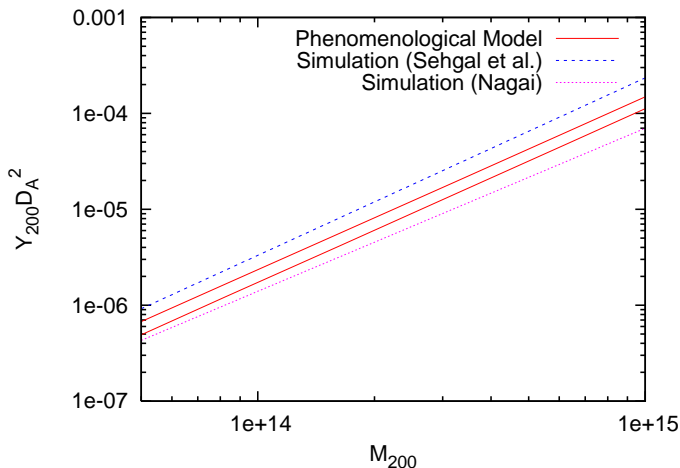


**Figure 4.** Scaling relation of  $Y_{200} D_A^2 - M_{200}$  of our phenomenological model (Solid line) and two simulations—Sehgal et al. (2007, dashed line) and Nagai (2006, dotted line). The upper solid line is  $Y_{200}$  over a cylindrical region in the same way as computed in Sehgal et al. (2007), while the lower line is that over a sphere in the same way as computed in Nagai 2006. The redshift is set to be 0 here.

2 in Sehgal et al. (2007), since we focus on clusters above the SZ detection threshold (about  $3 \times 10^{14} M_{\odot}$  at intermediate redshifts). Sehgal et al. find a slightly steeper slope than Nagai, which they attribute to the effect of AGN heating. The slope of Nagai roughly agrees with the self-similar expectation. Our slope is closer to that of Sehgal et al., which includes star formation, and AGN feedback, but no cooling. Overall, the slopes, however, are close to one another, and our normalization falls between the predictions of the two simulations.

In addition to the 15 parameters fixed above, we also

allow for independent scatter in the  $Y - T$  and the  $Y - M$  relations. We chose a fiducial value of 10% for both (i.e.  $\sigma_i$  in eq. 18 and  $\sigma_{Y,M}$  in eq. 21 are both  $0.1Y$ ), motivated by the simulations of Nagai (2006), who finds an r.m.s. scatter between  $Y$  and  $M$  of 10-15%. The effect of a non-zero  $Y - M$  scatter on our results is two-fold. Scatter increases the number of detected cluster at a given flux threshold (because of the steep slope of the mass function, more clusters scatter from below the threshold to above it than vice-versa), which is helpful in constraining cosmology. On the other hand, scatter flattens the effective mass function, which degrades the information derivable from the shape of the mass function (as will be demonstrated in § 3 below, we find that the second effect dominates in the constraints from the cluster counts).

In summary, we conclude that our fiducial cluster structure model matches existing observations and simulations reasonably well, at least at low redshifts, and for the clusters above the expected detection threshold of future SZ surveys. This gives us confidence to use our adopted model parameterization to forecast cosmological constraints, and to study the effect of cluster structure uncertainties. Of course, in the future, as better data becomes available, it is possible (indeed likely) that modifying the parameterization of the cluster structure model will become necessary.

*Survey parameters.* Survey parameters include the following: sky coverage  $\Delta\Omega$ , frequency  $f$ , measurement noise  $\sigma_m$ , redshift range  $z_{\min} - z_{\max}$  and related parameters, such as redshift bin size and  $Y$  bin size. We adopt typical values relevant to upcoming SZ surveys for these parameters.

The sky coverage  $\Delta\Omega$  is set to be  $4,000 \text{ deg}^2$  which is the solid angle covered by SPT in 2 years. The frequency  $f$  is chosen to be  $145 \text{ GHz}$ , where the SZ signal reaches maximum decrement. Most surveys will observe in bands at multiple frequencies, in order to separate the SZ signal from other CMB secondary anisotropies and from foregrounds. However, almost all planned surveys have a frequency band around  $145 \text{ GHz}$ . The detector noise  $\sigma_m$  is set to be  $1 \text{ mJy}$ , which represents a typical value for the total SZ flux of the smallest detectable cluster in upcoming surveys (such as in SPT). At frequency of  $145 \text{ GHz}$ , this corresponds to  $\sigma_m = 9.36 \times 10^{-13} \text{ sr}$ . We set the cluster detection threshold to be  $5\sigma_m$ . At low redshift, surface brightness becomes an important additional detection criterion, and a simple flux limit becomes inadequate, so we impose a floor on the mass limit  $M_{\min} = 10^{14} h^{-1} M_{\odot}$  (eq. 20). We will discuss how this choice affect our result in § 4.

We further assume the SZ survey covers the redshift range  $0.0 < z < 2.0$ , and we divide this range into 40 uniform bins ( $\Delta z = 0.05$ ). This of course requires the cluster redshift measurement uncertainty is better than 0.05. This accuracy should be achievable by follow-up surveys designed for this purpose; for example, the Dark Energy Survey can determine cluster photometric redshifts to an accuracy of 0.02 or better out to  $z \sim 1.3$  (Abbott et al. 2005).

Finally, we divide the  $Y$  range into 8 bins, which we allocate so that each bin contains a similar number of clusters. This requirement led us to adopt the following boundaries of the  $Y$ -bins, in units of the  $5\sigma_m$  detection threshold:  $[1 - 2^{1/4}]$ ,  $[2^{1/4} - 2^{1/2}]$ ,  $[2^{1/2} - 2^{3/4}]$ ,  $[2^{3/4} - 2^{1.0}]$ ,  $[2^{1.0} - 2^{5/4}]$ ,  $[2^{5/4} - 2^{3/2}]$ ,  $[2^{3/2} - 2^{7/2}]$ ,  $[2^{7/4} - \infty]$ .

In Figure 5, we show the minimum mass detectable by

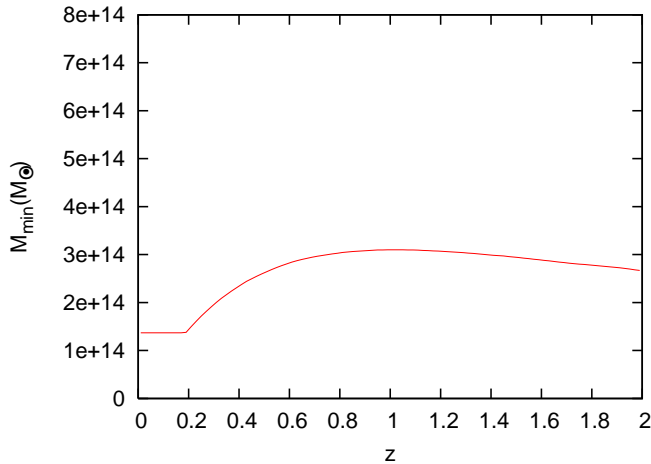


**Figure 5.** The mass of the smallest detectable cluster as function of redshift (neglecting scatter), corresponding to a constant SZ flux of 5 mJy. The flat part at low redshift is an additional constant mass limit imposed by hand,  $10^{14}h^{-1}M_{\odot}$ .

the SZ survey as function of redshift, neglecting scatter between  $Y$  and  $M$ . The flat portion of the curve at low redshift is the limit imposed by hand ( $10^{14}h^{-1}M_{\odot}$ ). The total number of detected clusters is about 6,800 for our adopted set of fiducial cosmological parameters (for reference, we note that the total number would be a factor of  $\sim 3$  higher,  $\approx 20,000$ , if we instead adopted the 1st year WMAP cosmological parameters; the difference attributable mostly to the change in  $\sigma_8$  from 0.90 to 0.76).

In our fiducial calculation, we assume that temperature measurements are available for all clusters detected by the SZ survey. This is usually taken to require X-ray spectroscopic data for each cluster. Mroczkowski et al. (2008) find that a joint analysis of SZ and X-ray imaging data, for 3 clusters detected with the SZA instrument, yields temperature profiles that are in good agreement with spectroscopic X-ray measurements. This may ease the requirement on the depth of the X-ray survey. The availability of temperatures for a large fraction of the SZ clusters may, however, still be an optimistic assumption, since the X-ray flux drops much faster than SZ flux at high redshift. We discuss the effect of partial followup in § 4.

### 3 RESULTS

With the cluster model and the Fisher matrix technique described above, we are now ready to forecast constraints from upcoming SZ and X-ray surveys. As an academic exercise, in § 3.1 we first consider an “idealized case”, in which cluster parameters are precisely known, and only cosmological parameters are constrained. This exercise serves two purposes: (i) it allows us to understand where the cosmology sensitivity comes from, and (ii) it will clarify the amount of the degradation in the constraints, once the cluster model parameter uncertainties are included. In § 3.2, we relax the assumption that cluster structure parameters are known, and simultaneously constrain cosmological and cluster parameters. Finally, in § 3.3, we investigate the effects of the additional uncertainties in the scatter and incompleteness.

#### 3.1 Constraints with cosmological parameters alone

Table 1 lists the marginalized  $1\sigma$  errors on cosmological parameters. In this and in the other tables below, “SR” stands for “scaling relations”, and “NC” stands for “number counts”. In addition to the marginalized errors (computed as  $\sigma = \sqrt{(F^{-1})_{ii}}$ ), in Table 1 we also list the single-parameter errors  $(F_{ii})^{-1/2}$ , and the degeneracy parameter  $\mathcal{D}$ , which we define as  $\sigma/(F_{ii})^{-1/2}$ . In the limit of no degeneracies,  $\mathcal{D} \rightarrow 1$ , while large  $\mathcal{D}$  indicates significant degeneracy.

As Table 1 shows, the scaling relation in general has a constraining power comparable to the number counts. For some of the cosmological parameters, and especially for  $w_0$  and  $w_a$ , the SR is even more powerful than the NC approach. This might be surprising, since the cluster abundance is known to be exponentially sensitive to cosmological parameters, while the SR depends on these parameters more-or-less “linearly”. However, the scaling relation approach has its own advantages. We compare these two approaches in more detail in § 4. Let us first see where the constraints come from in the scaling relation approach.

It is easy to see from equation (16) above that

$$Y \propto D_A^{-2} M_g T \sim D_A^{-2} f_g M_{\text{vir}} T. \quad (27)$$

Since we are studying the  $Y - T$  relation, we eliminate the mass  $M_{\text{vir}}$  from this equation by converting  $M_{\text{vir}}$  to  $T$  and  $\rho_{\text{vir}}$  using the virial theorem and mass conservation,

$$T_{\text{vir}} \propto M_{\text{vir}}/R_{\text{vir}} \quad (28)$$

$$M_{\text{vir}} \propto \rho_{\text{vir}} R_{\text{vir}}^3. \quad (29)$$

Combining the above three equations, we find

$$Y \propto D_A^{-2} f_g \rho_{\text{vir}}^{-1/2} T^{5/2}. \quad (30)$$

Equation (30) indicates that the dependence on cosmological parameters can arise through three terms: the angular diameter distance  $D_A$ , the gas fraction  $f_g$  (defined in § 2.2 above), and the virial overdensity  $\rho_{\text{vir}}$ . Here  $f_g$  and  $\rho_{\text{vir}}$  are both related to cluster properties;  $D_A$ , on the other hand, is a direct property of space-time geometry. Below, we first study the dependence of  $Y - T$  through the grouped combination of  $f_g \rho_{\text{vir}}^{-1/2}$  and through  $D_A^{-2}$ . This grouping is useful because  $D_A$  is a pure geometrical quantity, and the cosmology-dependence that arises through this quantity is likely to be quite robust. On the other hand, predicting  $f_g \rho_{\text{vir}}^{-1/2}$  requires a structure formation model, and the cosmology dependence through this quantity will be necessarily model dependent. In particular, while  $\rho_{\text{vir}}$  depends only on the details of nonlinear gravitational collapse,  $f_g$  also depends on gas physics – in particular, in our case, on our assumption of hydrostatic equilibrium. For each cosmological parameter, we want to know whether these two dependencies work in the same direction, or whether they tend to cancel each other – and, in either case, it is useful to know which dependence dominates the constraints.

To answer this question, we computed  $d \ln Y / dp$  separately from each cosmology-dependent term, since the Fisher matrix element (eq. 18) is proportional to this derivative. First, we allow cosmological parameters to vary when we compute  $D_A$ , but artificially keep them at their fiducial values in the computation of  $f_g$  and  $\rho_{\text{vir}}^{-1/2}$ . The resulting  $d \ln Y / dp$  quantifies the dependence through  $D_A^{-2}$  alone. We

**Table 1.** Estimated  $1\sigma$  errors on the cosmological parameters in the academic case when cluster structure parameters are precisely known. Here “SR” and “NC” stand for “scaling relation” and “number counts”, respectively. The degeneracy parameter  $\mathcal{D}$  is defined as  $\sigma/(F_{ii})^{-1/2}$ , so that large values indicate significant degeneracy.

Parameter constraints	SR			NC			Combined			$\xi^\dagger$
	$\sigma$	$(F_{ii})^{-1/2}$	$\mathcal{D}$	$\sigma$	$(F_{ii})^{-1/2}$	$\mathcal{D}$	$\sigma$	$(F_{ii})^{-1/2}$	$\mathcal{D}$	
$\Omega_m$	0.055	0.00030	183.4	0.023	0.0024	9.6	0.009	0.00029	29.6	0.17
$\Omega_{DE}$	0.20	0.028	7.0	0.29	0.016	18.4	0.06	0.014	4.32	0.13
$\Omega_b$	0.012	0.00006	189.7	0.007	0.00035	20.2	0.0037	0.00006	60.4	0.36
$h$	0.08	0.0014	55.1	0.11	0.006	18.6	0.050	0.0014	36.4	0.62
$w_0$	0.037	0.010	3.6	0.20	0.018	11.1	0.016	0.009	1.8	0.20
$w_a$	0.21	0.044	4.7	1.4	0.10	14.4	0.11	0.040	2.7	0.29
$\sigma_8$	N/A	N/A	N/A	0.016	0.0011	14.2	0.007	0.0011	6.2	0.19
$n_s$	N/A	N/A	N/A	0.13	0.023	5.7	0.036	0.022	1.6	0.08

$^\dagger$  “Complementarity” parameter which quantifies the level of degeneracy breaking when different measurements are combined. See eq. 31 and Fang & Haiman (2008) for the formal definition. for details.

next allow cosmological parameters vary in  $f_g$  and  $\rho_{\text{vir}}^{-1/2}$ , but we keep them fixed in  $D_A$ ; this yields the dependence through  $f_g\rho_{\text{vir}}^{-1/2}$  alone.<sup>7</sup> The overall dependence  $d\ln Y/dp$  is simply the sum of these two. We compute the above derivatives at  $z = 0.2$  and  $z = 1.5$  and the mass is set to  $10^{15}M_\odot$  (we did not find a strong mass dependence in the derivatives, so these numbers are typical for clusters in the whole mass range of interest).

The results of the above exercise are listed in Tables 2 and 3. As we can see from these two Tables, for each of the cosmological parameters, the derivative through  $D_A^{-2}$  and  $f_g\rho_{\text{vir}}^{-1/2}$  have different signs (except for  $\Omega_b$ , to which  $D_A$  has no sensitivity). This, unfortunately, means that the dependence from  $D_A^{-2}$  always cancels with the dependence from  $f_g\rho_{\text{vir}}^{-1/2}$ . For  $\Omega_m$  and  $\Omega_b$ , the overall derivative is driven overwhelmingly by  $f_g\rho_{\text{vir}}^{-1/2}$ , and correspondingly the constraints come through  $f_g\rho_{\text{vir}}^{-1/2}$ . For  $\Omega_{DE}$  and  $h$ , there are significant cancellations, and the overall derivative has the same sign as that from  $D_A^{-2}$ , so the constraints come predominantly through  $D_A^{-2}$ . For  $w_0$  and  $w_a$ , there are again significant cancellations, and the overall constraints come predominantly through  $f_g\rho_{\text{vir}}^{-1/2}$  at low redshift, but through  $D_A^{-2}$  at high redshift.

Although each parameter has a dependence through  $f_g\rho_{\text{vir}}^{-1/2}$ , the situation is different for  $(\Omega_m, \Omega_b)$  and for  $(w_0, w_a)$ .  $\Omega_m$  and  $\Omega_b$  are both directly related to  $f_g$ , while they have a smaller or no effect on  $\rho_{\text{vir}}$ . The gas fraction  $f_g$  is roughly proportional to the global baryon fraction  $f_b = \Omega_b/\Omega_m$ . This direct dependence is the strongest among all dependencies of  $Y - T$  on cosmological parameters. The dark energy equation-of-state parameters  $w_0$  and  $w_a$ , on the other hand, have no direct effect on  $f_g$ , and they mainly come into play through  $\rho_{\text{vir}}$ . A higher  $w$  induces a higher  $\rho_{\text{vir}}$ , because clusters collapse earlier in such a universe (Kuhlen et al. 2005). Higher density means higher temperature for given cluster mass (eqs. 28 and 29), or conversely, lower

<sup>7</sup> Although we will keep referring to the combination  $f_g\rho_{\text{vir}}^{-1/2}$ , it is useful to clarify that for  $w$ , the dependence through  $\rho_{\text{vir}}$  is always much stronger than the mild cosmology-dependence through  $f_g$  arising from eq. (9). On the other hand, we find that  $f_g$  is much more sensitive to  $\Omega_m$  and  $\Omega_b$  than  $\rho_{\text{vir}}$ .

**Table 2.**  $d\ln Y/dp$  evaluated at a fixed cluster temperature at  $z = 0.2$ , where  $p$  is any of the 6 cosmological parameters. The three columns, from left to right, show the values when we include the dependence only via  $D_A^{-2}$ , or only via  $f_g\rho_{\text{vir}}^{-1/2}$ , or the full derivative.

Parameter	$D_A^{-2}$	$f_g\rho_{\text{vir}}^{-1/2}$	Overall
$\Omega_m$	+0.13	-6.20	-6.07
$\Omega_{DE}$	-0.19	+0.15	-0.03
$\Omega_b$	0	+27.50	+27.50
$h$	+2.59	-1.34	+1.25
$w_0$	+0.19	-0.38	-0.19
$w_a$	+0.01	-0.05	-0.04

**Table 3.** Same as Table 2 except for  $z = 1.5$ .

Cosmological parameters	$D_A^{-2}$	$f_g\rho_{\text{vir}}^{-1/2}$	Overall
$\Omega_m$	+0.11	-6.75	-5.64
$\Omega_{DE}$	-0.76	+0.68	-0.08
$\Omega_b$	0	+26.96	+26.96
$h$	+2.59	-1.37	+1.23
$w_0$	+0.45	-0.15	+0.30
$w_a$	+0.11	-0.07	+0.03

mass for a given temperature. As a result,  $Y$  is reduced for a given  $T$  (eq. 27). This reduction is further enhanced by the indirect effect of  $\rho_{\text{vir}}$  on  $f_g$  through the pressure boundary condition. This can be understood by recalling that the ICM is assumed to be confined by the external pressure of the infalling gas. This pressure is proportional to  $\Omega_b T/\Omega_m$  (eqs. 10 and 28). When the virial density is raised, the external pressure increases roughly linearly with the temperature, which implies that the gas density is approximately kept constant ( $P \propto \rho T$ ). The gas fraction, which is roughly proportional to the ratio of gas density to the virial overdensity, is therefore reduced.

Among the cosmological parameters, the  $Y - T$  relation is most sensitive to  $\Omega_m$  and  $\Omega_b$ , and constraints on these two parameters are therefore the tightest. However

they also suffer the most from the severe degeneracy between one another (see column  $\mathcal{D}$  in Table 1). This is because both parameters affect the  $Y - T$  relation in an approximately uniform way, insensitive to redshift and cluster mass. This also means that a prior on one of these two parameters from another measurement could greatly help constrain the other. For example, if we apply a prior of 0.0015 from the result of WMAP+BAO+SN on  $\Omega_b$  (Dunkley et al. 2008),  $\Delta\Omega_m$  is reduced by more than a factor of 3, while the constraints on other parameters change only mildly. From the simple argument that both  $\Omega_m$  and  $\Omega_b$  are constrained through  $f_g$  and  $f_g$  is roughly proportional to the baryon fraction  $\Omega_b/\Omega_m$ , one could conclude that it is the combination  $\Omega_b\Omega_m^{-1}$  that is being constrained. This conclusion is borne out by our numerical results, which show that the direction of the Fisher eigenvector in the  $\Omega_b - \Omega_m$  subspace is in the direction  $\Omega_b\Omega_m^{-1.2} = \text{const}$ ; i.e., the scaling relation indeed best constrains this combination. Other parameters have a comparatively smaller effect on the  $Y - T$  relation (see the ‘‘Overall’’ column in Tables 2 and 3 and the corresponding column  $(F_{ii})^{-1/2}$  in Table 1). But due to the sensitivity to each parameter having a different redshift dependence, they suffer much weaker degeneracies. The parameter with the lowest degeneracy (smallest  $\mathcal{D}$  parameter) is  $w_0$ , with  $\mathcal{D} = 3.6$ , less than 1/50th of the degeneracy between  $\Omega_m$  and  $\Omega_b$ .

Analogous to the discussion above, previous works have clarified the cosmology-dependence of the cluster number counts. We refer the reader to, e.g., Haiman et al. (2001) for a detailed discussion; here we just emphasize two points. First, the number counts also include a cosmology-dependence from the  $Y - M$  relation, through the selection function  $g(Y_\alpha, M)$ . The number-count constraint on  $\Omega_b$  is driven through this dependence, but the constraints on other parameters are dominated by either the cosmological volume element or the growth function (except the  $\Omega_m$  dependence, which is dominated by the explicit linear scaling of the cluster mass function with  $\Omega_m$ ). Second, we not only have multiple redshift bins, but also multiple  $Y$ -bins. This helps significantly in constraining cosmological parameters (analogously to the shape of the cluster mass function being helpful; e.g., Hu 2003). In Table 4 below, we present constraints both with and without binning in  $Y$ . Comparing these two cases, we see that the  $\mathcal{D}$  parameter changes significantly, while  $(F_{ii})^{-1/2}$  has only a mild change. This shows that the tightening of the constraints in the case when 8  $Y$  bins are used is achieved mainly via breaking degeneracies between different parameters. In the same table, we also list constraints when the scatter between  $Y$  and  $M$  is set to zero. The constraints become more stringent, which highlights the degrading effect of the  $Y - M$  scatter through flattening the mass function. A small scatter in the mass-observable relation (10% as assumed in this work) is seen to degrade constraints by a factor of up to 4 (the parameter  $h$ ). Again, we see that this is mainly due to higher degeneracies in the presence of the scatter.

### 3.2 Constraints with cosmological and cluster parameters

Below, we consider the more ‘‘realistic’’ case, in which we take into account uncertainties in cluster structure and its

evolution. In § 2.2, we have parameterized cluster structure and evolution with 15 parameters, characterizing various aspects of ICM physics, namely the shape of the gravitational potential, the gas entropy, non-thermal pressure, and boundary condition, as well as the mass- and redshift-dependence of these parametrized quantities. We repeat the above analysis, but also including these cluster structure parameters, which means we constrain 23 parameters simultaneously. The results of this exercise are shown in Table 5. Within the parentheses next to the errors on the cosmological parameters, we list the ratio of errors,  $\mathcal{R} = \sigma_2/\sigma_1$ , where  $\sigma_1$  is the idealized constraint shown in Table 1, and  $\sigma_2$  is the new value in Table 5. This ratio  $\mathcal{R}$  therefore quantifies the degradation of the constraint introduced by the cluster parameter uncertainties. For the majority of parameters, the degradation is less than a factor of 2, and the constraints remain tight, despite the large increase in parameter space (this is true for both the scaling relation and number counts approaches). We emphasize again that we simplified things by assuming a particular form (eqs. 11) for the mass and redshift dependence of cluster parameters; nevertheless, these results highlight the ability of upcoming surveys to constrain a large number of parameters, which is due essentially to the large number of clusters and therefore small statistical errors.

For the number counts approach, the largest degradation is on  $\Omega_b$ . This is understandable, because unlike for other cosmological parameters, the constraint on  $\Omega_b$ , as we have mentioned, is largely from the  $Y - M$  relation in eq. (21), not from the mass function itself, and all of the 15 cluster parameters affect the  $Y - M$  relation. This could account for the large degeneracy between  $\Omega_b$  and the cluster parameters. Of course,  $\Omega_b$  is measured accurately by other methods (Kirkman et al. 2003; Dunkley et al. 2008), and this degradation is not a concern. In the scaling relations, however, the largest degradation is suffered by  $w_0$ . This is because the simple power-law parameterization in eq. 11 happens to be close to the way  $w_0$  affects the evolution of the scaling relation. This large degeneracy between the DE equation-of-state parameters and cluster parameter suggests that the cluster constraints on  $w_0$  and  $w_a$  will be especially useful when combined with independent measurements of these parameters using other probes.

Table 5 shows further that the constraints on cluster parameters are, in general, quite weak from both approaches, with most constraints at the order-unity level. This, conversely, indicates that the  $Y$  parameter is relatively insensitive to cluster parameter variations. We see from Table 5 that the single-parameter errors  $(F_{ii})^{-1/2}$  for the cluster parameters are very low, showing that the weakness of these constraints are due to strong degeneracies among the cluster model parameters. One likely reason for this strong degeneracy is that we adopted the same power-law form for the mass- and redshift-evolution for each of the cluster parameters. Indeed, we find that introducing even unrealistically tight priors on the cosmological parameters do not improve cluster parameter constraints significantly, indicating that the degeneracies are among the cluster parameters themselves. We thus conclude that  $Y - T$  relation by itself is not a good way of placing precise constraints on individual cluster parameters, unless the mass-dependence and redshift-evolution of the physical parameters can be

**Table 4.** Constraints from number counts approach with different scatter and different number of  $Y$  bins. Columns labeled with “Fiducial” contain results with 10% scatter and 8  $Y$  bins; columns labeled with “1  $Y$  bin” contain results with 10% scatter and 1  $Y$  bin; columns labeled with “No Scatter” contain results with no scatter and 8  $Y$  bins.

Parameter constraints	Fiducial			1 $Y$ bin			No Scatter		
	$\sigma$	$(F_{ii})^{-1/2}$	$\mathcal{D}$	$\sigma$	$(F_{ii})^{-1/2}$	$\mathcal{D}$	$\sigma$	$(F_{ii})^{-1/2}$	$\mathcal{D}$
$\Omega_m$	0.023	0.0024	9.6	0.10	0.0026	39.4	0.018	0.0022	8.1
$\Omega_{DE}$	0.29	0.016	18.4	1.0	0.016	63.0	0.19	0.015	12.5
$\Omega_b$	0.007	0.00035	20.2	0.042	0.00043	99.2	0.0019	0.00030	6.4
$h$	0.11	0.006	18.6	0.54	0.007	75.9	0.028	0.0049	5.6
$w_0$	0.20	0.018	11.1	0.42	0.019	22.5	0.12	0.017	7.0
$w_a$	1.4	0.10	14.4	8.1	0.10	80.3	1.0	0.10	9.9
$\sigma_8$	0.016	0.0011	14.2	0.07	0.0011	66.5	0.011	0.0011	10.3
$n_s$	0.13	0.023	5.7	1.1	0.037	28.6	0.06	0.022	2.9

understood a-priori, and they differ significantly from the power-law forms assumed here. Of course, the  $Y - T$  relation still delivers tight constraints on cluster-parameter combinations, so it should be useful when combined with other cluster observables.

### 3.3 Effects of scatter and completeness uncertainties

In addition to the uncertainties in cluster structure, there are also uncertainties in scatter and completeness. The scaling relation test is affected by scatter and incompleteness only indirectly through Malmquist bias. This bias is the increase in the mean value of  $Y$  at fixed  $T$ , because the lowest- $Y$  clusters that are scattered below the detection threshold are missing from the sample. We find that the scatter changes the number of detectable clusters in each redshift bin by less than 1% (except in the three bins beyond  $z = 1.8$ , where the changes are between 1-2%), and the mean  $\langle Y \rangle$  is changed by a similar amount. This is comparable to the change in  $\langle Y \rangle$  caused by variations in our parameters within their marginalized  $1\sigma$  uncertainties (see Tables 2, 3 and 1). However, since flux limited surveys can do a correction that should eliminate the bulk of the Malmquist bias, we believe this will not be a major limitation of the constraints.

The effects of scatter and completeness uncertainties on the number counts constraints is somewhat more subtle. In this section, we allow both the scatter and a completeness to vary, together with the cosmological and cluster parameters. The scatter between  $M$  and  $Y$  is parameterized using the same power-law form as the cluster parameters (eq. 11). The completeness  $\mathcal{C}$ , defined as the fraction of clusters at a given  $Y$  at redshift  $z$  that are detected is taken to be given by a similar power-law, except  $M/M^*$  is replaced by  $Y/Y^*$  in equation (11), where  $Y^*$  is chosen to be  $1mJy$ .

The fiducial scatter is assumed to be 10%, and the fiducial completeness is set to be 100% (both independent of redshift and mass, except completeness is set to zero below  $M_{\min}$ ). Table 6 shows the results when scatter is included and when both scatter and incompleteness are included. For comparison, we also list the result when neither uncertainty is taken into account (repeating the NC column from Table 5). The degradations are relatively small for most parameters. The two exception are  $\Omega_m$  and  $\sigma_8$ , for which the number-count constraints degrade by a factor of  $\sim 3$  when

the completeness uncertainty is included. The impact of the completeness uncertainty is relatively modest, because our treatment assumes that we know the form of the dependence of  $\mathcal{C}$  on  $Y$  and  $z$  (i.e. power-laws in our case). At the opposite extreme, if one allows completeness to be an arbitrary function of mass and redshift, then of course no constraint can be derived on any model parameter. The fact that we still find interesting constraints shows that a reliable parameterization of the completeness as a function of  $Y$  and  $z$  will be very important. We also find that all of the constraints would recover their values (to within 30%) in the fixed  $\mathcal{C} = 1$  case when a prior of 15% is applied to  $\mathcal{C}$ . Finally, in Table 6, we also list the combined constraints from the scaling relations and the number counts. Comparing these values with the combined constraints listed in Table 5, we find that these constraints are less affected by incompleteness than those from number counts approach alone. Except for  $\sigma_8$ , which degrades by a factor of  $\sim 2$ , the constraints all degrade by factors of  $\lesssim 1.5$ .

The physical origin of scatter in the observables  $Y$  and  $T$  can be cluster-to-cluster variations in the structure parameters (even in the context of our idealized spherical models), and geometrical effects (i.e. viewing aspherical clusters along different sight-lines). As mentioned in § 2.2 above, in addition to the Malmquist bias, underlying scatter in a physical structure parameter can cause a bias by producing a skewed probability distribution for  $Y$ . In order to assess how large this additional bias might be, we have performed the following calculation. First, looking at the third column in Table 5, we see that the best constrained individual cluster parameter is  $s_{\text{norm}}$ . This suggests that among the cluster structure parameters, it is this parameter (the slope of the entropy profile) that could cause the largest bias. We then assumed a symmetric, Gaussian scatter on this parameter, with an r.m.s. equal to 10% of its fiducial value ( $\sigma_{s_{\text{norm}}} = 0.11$ ). We then computed the distribution of  $Y$ -values, for clusters at  $z = 0.5$ , and  $T = 7\text{keV}$ , induced by this Gaussian scatter<sup>8</sup>. In the absence of any scatter in  $s_{\text{norm}}$ , the mean SZ decrement at  $T = 7\text{keV}$  is  $\langle Y \rangle = 70.46mJy$ . When the scatter is included, we find that  $\langle Y \rangle$  is increased by 2%, to 71.88 mJy.

<sup>8</sup> Note that changes in  $s_{\text{norm}}$  change both  $Y$  and  $T$ ; since we are interested in the distribution of  $Y$  at fixed  $T$ , we adjust the cluster mass  $M$ , for each value of  $s_{\text{norm}}$ , to keep  $T$  fixed at 7 keV.

**Table 5.** Constraints as in Table 1, except in the more realistic case that includes cluster structure parameters. Within the parentheses next to the errors on each cosmological parameter, we list the factor by which the constraints degrade relative to the idealized case.

Parameter	SR		NC		Combined		
	$\sigma$	$(F_{ii})^{-1/2}$	$\sigma$	$(F_{ii})^{-1/2}$	$\sigma$	$(F_{ii})^{-1/2}$	$\xi$
$\Omega_m$	0.087(1.6)	0.00030	0.068(2.9)	0.0024	0.038(4.2)	0.00030	0.50
$\Omega_{DE}$	0.28(1.4)	0.029	0.34(1.2)	0.016	0.15(2.5)	0.014	0.46
$\Omega_b$	0.080(6.7)	0.000062	0.10(14.3)	0.00035	0.038(10.3)	0.000061	0.38
$h$	0.12(1.5)	0.0014	0.14(1.3)	0.0060	0.075(1.5)	0.0014	0.70
$w_0$	0.53(14.3)	0.010	0.34(1.7)	0.018	0.22(13.8)	0.0089	0.58
$w_a$	0.64(3.0)	0.044	1.63(1.2)	0.099	0.45(4.1)	0.040	0.58
$\sigma_8$	N/A	N/A	0.055(3.4)	0.0011	0.033(4.7)	0.0011	0.36
$n_s$	N/A	N/A	0.87(6.5)	0.023	0.46(12.8)	0.023	0.28
$\hat{K}_{\text{norm}}$	4.37	0.0042	2.25	0.020	0.56	0.0041	0.08
$\hat{K}_m$	0.67	0.0014	0.96	0.010	0.24	0.0014	0.19
$\hat{K}_z$	1.95	0.0048	2.03	0.022	0.79	0.0047	0.32
$s_{\text{norm}}$	0.98	0.00092	2.40	0.0097	0.57	0.00092	0.40
$s_m$	0.075	0.00061	1.75	0.010	0.042	0.00061	0.32
$s_z$	0.96	0.0024	3.56	0.023	0.48	0.0024	0.27
$b_{\text{norm}}$	3.54	0.0063	2.60	0.014	1.02	0.0057	0.24
$b_m$	1.92	0.0050	1.83	0.015	0.73	0.0048	0.30
$b_z$	0.011	0.0026	0.26	0.0093	0.0083	0.0025	0.61
$c_{\text{norm}}^{\text{NFW}}$	2.02	0.0030	6.67	0.076	1.03	0.0030	0.29
$c_m^{\text{NFW}}$	1.05	0.0024	6.59	0.10	0.49	0.0024	0.22
$c_z^{\text{NFW}}$	2.47	0.0085	5.74	0.25	1.33	0.0085	0.35
$\eta_{\text{norm}}$	0.85	0.0016	0.45	0.0050	0.18	0.0015	0.20
$\eta_m$	0.97	0.0015	0.85	0.0062	0.24	0.0015	0.14
$\eta_z$	1.09	0.0049	1.33	0.013	0.47	0.0046	0.31

This level of bias is certainly a concern. From the parameter constraints  $\sigma(p)$  listed in Table 1, and the logarithmic dependencies of  $Y$  vs  $p$  listed in Tables 2 and 3, we infer that systematic errors on the measurement of  $\langle Y \rangle$  at fixed  $T$  should be controlled to within  $\approx 1\%$ , in order for the corresponding bias on the parameters not to exceed the  $1\sigma$  constraints. Furthermore, in the above exercise, we find a standard deviation of  $\sigma(Y) = 14 \text{ mJy} = 0.194\langle Y \rangle$ ; i.e. a value that is almost double the fiducial adopted 10% scatter in the  $Y - T$  relation. These numbers suggests that, in order to realize constraints comparable to the forecasts we present here, it will be necessary to obtain a physical understanding of the scatter in cluster-structure from hydrodynamical simulations. When the technique proposed here is applied to an actual large data-set, it will be important to include parameters that describe such scatter. The full distribution of  $Y$  at fixed  $T$ , rather than the single value  $\langle Y \rangle$ , can then be used as additional signal, in order to constrain these extra parameters.

## 4 DISCUSSION

### 4.1 Comparing the $Y - T$ and $dN/dz$ Constraints

We have forecast the constraints from  $Y - T$  scaling relation approach and number counts approach. Interestingly, we find that these two approaches yield comparable results, even though the cluster abundance is more sensitive to cosmological parameters than the scaling relation. There are several reasons, however, for the scaling relations to be competitive, at least statistically. First, the number counts only utilize  $Y$  and  $z$  of a cluster, while the scaling relation also

derives information from the temperature  $T$ . Second, in the scaling relations, each cluster adds a new data point, so that we are effectively using  $N \approx 6,800$  independent measurements of the observable  $Y$ . Each  $Y$ -measurement has a fractional error significantly below order unity (of order  $\Delta Y/Y = \sigma_{Y,T} \approx 20\%$  in eq. 18), so that when these are combined independently, the effective combined statistical error is  $\sigma_{Y,T}/\sqrt{N}$ . This is better than the total effective Poisson error ( $\sim \sqrt{N}$ ) from the cluster counts. This statement holds as long as  $Y$  is measured at fixed  $T$  with an uncertainty better than order unity, since effectively, in the number count approach, each cluster contributes an order-unity statistical error. This comparison neglects systematic errors, which can ultimately limit the constraints from both approaches. In particular, systematic errors in both the measurements of  $Y(T)$  and its model predictions have to be at the  $\lesssim 1/\sqrt{N} \approx 1\%$  level, in order not to dominate over the statistical errors; likewise, selection effects for the cluster counts have to be controlled to this level of systematic accuracy. Third, unlike cluster counts, the scaling relation does not explicitly depend on  $\sigma_8$  and  $n_s$ . The only dependence is through the Malmquist bias, but we find this dependence to be negligibly small, even when varying  $\sigma_8$  in the range of 0.7-0.9. Therefore, the scaling relation avoids degeneracies involving these parameters. Finally, as mentioned above, the number counts approach is less robust to selection errors.

Quantitatively, the scaling relation approach yields tighter constraints on  $\Omega_{DE}$ ,  $h$ ,  $w_0$  and  $w_a$  when the uncertainty in cluster structure is ignored, while the number counts do better for the other parameters. Once we include cluster structure uncertainty, the constraint on  $w_0$  from the

**Table 6.** Constraints from number counts approach with scatter and incompleteness taken into account. First column is the result when the uncertainties on scatter and completeness are ignored; second column is the result when the uncertainty on scatter is included; third column is the result when both uncertainties are taken into account; lastly we also list the combined constraints from number counts approach and scaling relation approach with scatter and incompleteness included.

Parameter	None NC	+S <sup>†</sup> NC	+S+I <sup>†</sup> NC	+S+I <sup>†</sup> Combined	ξ
$\Omega_m$	0.068	0.072	0.225	0.060	0.55
$\Omega_{DE}$	0.34	0.35	0.66	0.22	0.72
$\Omega_b$	0.10	0.12	0.12	0.053	0.65
$h$	0.14	0.17	0.18	0.081	0.68
$w_0$	0.35	0.46	0.56	0.27	0.49
$w_a$	1.63	1.66	1.78	0.48	0.66
$\sigma_8$	0.055	0.061	0.17	0.072	0.19
$n_s$	0.87	0.92	1.08	0.64	0.35
$\hat{K}_{\text{norm}}$	2.25	2.73	2.78	1.41	0.36
$\hat{K}_m$	0.96	1.24	1.48	0.26	0.18
$\hat{K}_z$	2.03	2.08	2.12	0.91	0.40
$s_{\text{norm}}$	2.40	2.90	2.93	0.68	0.54
$s_m$	1.75	1.88	2.07	0.045	0.36
$s_z$	3.56	3.77	3.99	0.52	0.31
$b_{\text{norm}}$	2.60	3.11	3.16	1.16	0.24
$b_m$	1.83	2.17	2.33	0.86	0.34
$b_z$	0.26	0.44	0.45	0.0089	0.70
$c_{\text{norm}}^{\text{NFW}}$	6.67	7.25	7.66	1.45	0.55
$c_m^{\text{NFW}}$	6.59	6.99	7.42	0.57	0.30
$c_z^{\text{NFW}}$	5.74	6.08	7.18	1.38	0.35
$\eta_{\text{norm}}$	0.45	0.64	0.64	0.26	0.26
$\eta_m$	0.85	0.93	0.96	0.26	0.14
$\eta_z$	1.39	1.38	1.44	0.48	0.30
$\sigma_{\text{norm}}$		0.18	0.18	0.088	0.23
$\sigma_m$		7.60	7.79	3.77	0.23
$\sigma_z$		8.64	8.77	5.75	0.43
$C_{\text{norm}}$			1.72	0.56	0.11
$C_m$			0.13	0.088	0.46
$C_z$			2.68	1.14	0.18

<sup>†</sup> “S” stands for “Scatter”, “I” stands for “Incompleteness”.

scaling relations and  $\Omega_b$  from the number counts suffer bad degradations.

## 4.2 Combined $Y - T$ and $dN/dz$ Constraints

We also computed the combined constraints from the two methods. As stated above, we assume that the two constraints are independent, and simply add the Fisher matrices; we justify this assumption in § 4.11 below. Combining the scaling relation with the number counts is useful to break degeneracies. For example, in the idealized case, the combined constraint on  $n_s$  is a factor of 3 tighter than that from number counts alone. This improvement is entirely from degeneracy breaking, since the scaling relation approach does not directly constrain  $n_s$ . While the  $n_s$  constraints in the realistic case degrade to uninteresting levels, the degeneracy breaking is also helpful in constraining other parameters. To quantify this, we computed the “complementarity” parameter, which defined as (Fang & Haiman 2008),

$$\xi = (\Delta p^{\text{combined}})^2 \left[ \frac{1}{(\Delta p^{\text{sr}})^2} + \frac{1}{(\Delta p^{\text{nc}})^2} \right] \quad (31)$$

In the idealized case (Table 1), this parameter is below 0.2 for 5 of the 8 cosmological parameters, meaning that for these parameters, the combined constraints are more than a factor of two tighter than simply adding the two results in quadrature. This parameter is larger in the realistic case (Table 5), with an average of  $\sim 0.48$  for the cosmological parameters (the lowest value is 0.28, for  $n_s$ ).

## 4.3 Beyond Power-Law Cluster Structure Models

In Figure 1, we saw a hint that our power-law parameterizations (in eq. 11) might be insufficient over an extended mass (and possibly also redshift) range. Since the degeneracy between cosmological and cluster parameters depends on this explicit form, we investigated the impact of allowing “curvature” in these power-laws. Specifically, we modified equation (11) to include higher order terms,

$$\ln p = \ln p_{\text{norm}} + p_{m1} \ln \frac{M}{M^*} + p_{m2} \left( \ln \frac{M}{M^*} \right)^2 + p_{z1} \ln(1+z) + p_{z2} [\ln(1+z)]^2. \quad (32)$$

With the inclusion of these new terms, we have  $5 \times 5 = 25$  cluster model parameters. We use the Fisher matrix technique to forecast constraints on these 25 parameters, together with the cosmological parameters. Compared to the 15 cluster parameter case (Table 5), we find that the constraints on  $\Omega_m$ ,  $w_0$  and  $w_a$  are the most affected, with an increase in their marginalized errors by a factor of  $\approx 2$ . From the large degradation factors ( $\sim 10$ ) shown in the parentheses in Table 5, we see that  $\Omega_b$  is sensitive to cluster structure uncertainties, as well. However, we find that the constraints on  $\Omega_{DE}$  and  $h$  are relatively robust to these uncertainties. The reason is that, as shown above, the constraints on these two parameters arise through  $D_A$ , which is not affected by cluster parameters, while the constraints on all other parameters receive a significant contribution from the cluster properties. We also find that if we simultaneously impose a prior of 50% on the fractional error on each of the 25 cluster parameters, this recovers constraints similar to that of 15 cluster parameters case. This suggests that relatively weak priors may mitigate the impact of more complicated cluster structure models.

## 4.4 Uncertainties from the Low-Redshift Mass-Floor

At low redshifts, the mass corresponding to a simple constant SZ flux is very low – dropping below masses corresponding to galaxy clusters. The nearby objects extend a large solid angle, so that surface brightness selection effects are no longer negligible. While this issue can be addressed by using different cluster-finding algorithms (e.g., Sehgal et al. 2007), for simplicity, we have imposed a constant mass limit of  $10^{14} h^{-1} M_{\odot}$ .<sup>9</sup> To see whether the constraints are sensitive to the (somewhat arbitrary) choice of this mass floor, we re-computed our constraints for a different value of

<sup>9</sup> The selection will also be affected by instrumental specifications, such as the beam profile, which will have to be taken into account in an actual analysis.

$5 \times 10^{13} h^{-1} M_{\odot}$ . Lowering the mass floor increases the total number of clusters by  $\sim 13\%$  (i.e. by  $\sim 900$  new clusters at redshift below  $\sim 0.2$ , where the mass floor is above the mass limit set by the flux threshold). The scaling relation results are not very sensitive to this change; the difference in the constraints is only a few percent in the idealized case, and up to 20% in the realistic case. The results, however, change more significantly in the number counts approach. In the idealized case,  $\Omega_m$ ,  $\Omega_{DE}$ ,  $w_0$  and  $w_a$  are most affected – their constraints improve to 0.014, 0.080, 0.094 and 0.28 respectively (compared to the original results of 0.023, 0.29, 0.20 and 1.4). These large improvements cannot be explained by the modest,  $\sim 13\%$  increase in the number of clusters, implying that the low-redshift, low-mass clusters help break the significant degeneracies among these parameters. In the realistic case, lowering the mass floor by a factor of two still improves the constraints on  $(\Omega_m, \Omega_{DE}, w_0, w_a)$  by factors of (1.4, 1.9, 1.6, 4.6). This underscores the importance of an accurate measurement of the abundance of low-mass clusters at low redshifts. It also shows that mis-estimates in the value of the mass floor can potentially introduce a large bias; such mis-estimates are equivalent to errors in the selection function as discussed in § 3.3 above.

#### 4.5 Uncertainties from Excising the Cluster Core

A potential concern is that in our  $Y - T$  scaling relation, we restricted the definition of the emission-weighted temperature outside the radius  $0.15R_{500}$  (see eq. 17). While this eliminates the sensitivity of the temperature to the complex physics in the cluster core, it can still introduce uncertainties or a bias in the inferred  $T_{ew}$ , since the inner radius has to be estimated from the data itself. We can ask the simple question: how accurately do we have to know  $R_{500}$ , in order for the corresponding bias not to exceed the  $1\sigma$  constraints we obtained above? As mentioned in § 3.3 above, the systematic errors on the measurement of  $Y$  at fixed  $T_{ew}$  should be controlled to within  $\approx 1\%$ . Since  $Y \propto T_{ew}^{2.5}$  (see eq. 30), this implies that the systematics of the  $T_{ew}$  measurement has to be accurate to  $\approx 0.4\%$ . We emphasize that this is the required systematic error, and a much larger scatter on the measurements for individual clusters is tolerable (in our case, the individual temperatures need to be known to an accuracy of  $\sqrt{6,800} \times 0.4\% \approx 30\%$ ). We find that a 0.4% change in the temperature corresponds to a 5% change in the radius (i.e. in the lower limit of the integral in eq. 17; for reference, the difference between  $R_{600}$  and  $R_{500}$  is around 8%). The cosmological dependence of  $R_{500}$  is smaller than this: a  $1\sigma$  ( $=0.055$ ) change in  $\Omega_m$  induces a 3.5% change in  $R_{500}$ , and other cosmological dependencies are much weaker. We conclude that the cosmology-dependence of  $R_{500}$  will not degrade the errors by more than  $1\sigma$ . However, the 5% error in the radius, translates into a 15% systematic error requirement on the enclosed mass. It should be possible to calibrate the  $Y - M$  relation to within 15% systematic accuracy (Kravtsov et al. 2006), especially if  $\sim 10\%$  priors on  $\Omega_m$  and  $\Omega_b$  are used.

#### 4.6 Using Priors on Cluster Structure to Improve Constraints

In the realistic case above, we have arguably been pessimistic by allowing all of the cluster parameters to vary arbitrarily. In reality, useful priors may be available on these parameters, either from other observations, or from simulations. For example, detailed X-ray measurements already reveal ICM entropy profiles in low redshift clusters (Ponman et al. 2003, Pratt. et al. 2006). Likewise, the NFW concentration parameter has been carefully studied in numerical simulations (e.g., Navarro et al. 1997; Wechsler et al. 2002; Kuhlen et al. 2005). To assess whether such priors could improve constraints on cosmological parameters, in Table 7 we present the results of calculations that adopt a prior of 1.0 and 0.1 on the fractional errors on all cluster parameters. Arguably, order-unity priors should be achievable, and in this sense, the results in Table 7 are even more “realistic” than those without priors. While improvements are noticeable (approaching factors of two for  $w_0$  and  $w_a$ ) for the SR-only constraints even with these weak priors, Table 7 shows that improving the combined SR+NC constraints by a factor of two requires  $\sim 10\%$  priors.

In order to assess whether a single cluster parameter is the “culprit”, we next tried applying priors on individual cluster parameters. We found no significant improvements, even if we applied priors of 0.001 on any one of the cluster parameters. This shows that the degeneracies are all inherently multi-dimensional. As an another series of exercises, we applied simultaneous priors either on the set of all normalization parameters ( $\bar{K}_{norm}$ ,  $s_{norm}$ ,  $b_{norm}$ ,  $c_{norm}^{NFW}$ ,  $\eta_{norm}$ ), the set of all mass-dependence parameters, or the set of all redshift-dependence parameters. We focus on how these priors affect SR constraints on  $w_0$ , since this is the constraint most affected by the cluster parameters. We find that the largest improvements are afforded by priors on redshift-dependence parameters. The constraint improves from 0.53 to 0.25 when a prior of 0.1 is applied to all redshift dependence parameters.

#### 4.7 Beyond the Total SZ Decrement

Although large upcoming SZ surveys will not produce resolved images of a large fraction of the detected clusters, it should still be possible to go beyond measuring the overall SZ decrement, and to obtain at least a rough constraint on its profile. For example, for SPT and ACT, the expected angular resolution is  $1'$ , while clusters typically extend a few arc minutes. Given that our cluster model specifies the radial structure of the cluster, it is interesting to ask whether this additional information might help further constrain parameters. To see how large these improvements could be, we divided every cluster into two annular regions: an inner part with radius  $2'$ , and an outer part from  $r = 2'$  to the virial radius. We assumed the SZ survey could independently measure  $Y$  in both regions. The measurement errors are assumed to be proportional to the square root of their solid angles, and the sum in quadrature of the two errors is fixed to be 1 mJy (to be consistent with our preceding calculations, which adopted 1 mJy for the cluster as a whole). The Fisher matrix forecast that use both  $Y$  observables are given in Table 8, with and without cluster parameters in-

**Table 7.** Constraints from the scaling relations, using pessimistic or optimistic priors on cluster model parameters. Priors are applied simultaneously to all of the cluster parameters, but only the constraints on cosmological parameters are listed.

Parameter	Prior of 1				Prior of 0.1			
	SR	NC	SR+NC	$\xi$	SR	NC	SR+NC	$\xi$
$\Omega_m$	0.071	0.053	0.035	0.70	0.064	0.029	0.022	0.66
$\Omega_{DE}$	0.26	0.31	0.14	0.52	0.24	0.30	0.10	0.30
$\Omega_b$	0.047	0.047	0.030	0.80	0.016	0.012	0.0077	0.63
$h$	0.11	0.12	0.072	0.78	0.089	0.11	0.066	0.90
$w_0$	0.34	0.28	0.19	0.77	0.17	0.21	0.12	0.85
$w_a$	0.46	1.56	0.37	0.69	0.34	1.45	0.21	0.41
$\sigma_8$	N/A	0.044	0.032	0.52	N/A	0.023	0.017	0.52
$n_s$	N/A	0.61	0.40	0.43	N/A	0.27	0.22	0.71

**Table 8.** Constraints on cosmological parameters when the solid area of the cluster is divided into two annular regions, an inner part with angular radius  $2'$  and an outer part outside radius  $2'$ . The constraints assume the  $Y$  parameters in both regions are measurable independently. The columns  $\mathcal{R}$  list the ratio of these constraints to their corresponding values from Tables 1 and 5 which use a single  $Y$  parameter.

Parameter	6 parameters		21 parameters	
	$\sigma$	$\mathcal{R}$	$\sigma$	$\mathcal{R}$
$\Omega_m$	0.010	0.19	0.050	0.58
$\Omega_{DE}$	0.042	0.21	0.18	0.65
$\Omega_b$	0.0040	0.34	0.036	0.45
$h$	0.048	0.63	0.075	0.65
$w_0$	0.013	0.36	0.21	0.41
$w_a$	0.12	0.57	0.30	0.47

cluded. The columns  $\mathcal{R}$  list the ratio of the new constraints to their corresponding old values from Tables 1 and 5. As these ratios reveal, even the very crude measurement of the  $Y$  profile can improve the constraints by a factor of  $\sim 2$ .

#### 4.8 Spectroscopic Coverage

A significant caveat, mentioned above, is that full spectroscopic X-ray coverage of all SZ clusters is likely to be unavailable, since the X-ray flux scales with redshift as  $D_L^{-2}$ , rather than  $D_A^{-2}$  as SZ flux. For simplicity, we here study the effect of partial X-ray data, by discarding all clusters beyond  $z = 1$  from the scaling relations. The results are presented in Table 9, where again the columns  $\mathcal{R}$  list the ratio of these new constraints to their old values in Tables 1 and 5. It turns out that the degradation is small, when cluster structure uncertainty is neglected – the largest difference is in  $\Delta w_0$ , whose error increases from 0.037 to 0.05. When the cluster structure parameters are included, the degradation is more severe (a factor of 1.7 for  $w_0$ ). Given that the number of clusters beyond  $z = 1$  is only about 5% of the total, and that they can bring down the constraints by a factor of  $\sim 2$ , it could be worthwhile to conduct deep X-ray followup measurements of these  $\sim 300$  clusters at  $z > 1$ . We note here for reference that the eROSITA deep survey is planned to cover  $200 \text{ deg}^2$ ; acquiring  $\sim 30\%$  temperatures out to  $z = 1$ , and/or to follow up on  $\sim 300$  clusters at  $z > 1$  will be chal-

**Table 9.** Constraints from scaling relations up to  $z = 1$  only.

Parameter	6 parameters		21 parameters	
	$\sigma$	$\mathcal{R}$	$\sigma$	$\mathcal{R}$
$\Omega_m$	0.066	1.2	0.20	2.3
$\Omega_{DE}$	0.23	1.1	0.32	1.1
$\Omega_b$	0.014	1.2	0.21	2.7
$h$	0.081	1.1	0.13	1.1
$w_0$	0.050	1.4	0.92	1.7
$w_a$	0.23	1.1	1.11	1.8

lenging, but should be feasible in a large dedicated X-ray survey (e.g., Haiman et al. 2005). An alternative method may be to rely only on X-ray imaging data: Mroczkowski et al. (2008) find that a joint analysis of SZ and X-ray imaging data, for 3 clusters detected with the SZA instrument, yields temperature profiles that are in good agreement with spectroscopic X-ray measurements. This may significantly ease the requirement on the depth of the X-ray survey.

#### 4.9 Impact of Flat Universe Prior

We also note that most other forecasts in the literature tend to adopt a flat universe prior. When we impose this condition ( $\Omega_m + \Omega_{DE} = 1$ ), we find that our conclusions do not change significantly. In the idealized case without cluster parameters, we find that the NC-alone constraint on  $\Delta w_a$  is reduced from 1.4 to 0.47, and the SR-alone constraint on  $\Delta w_0$  is reduced from 0.037 to 0.012. These improvements, however are much less significant when cluster structure uncertainty is taken into account (the NC-alone constraint on  $\Delta w_0$  is reduced from 1.61 to 1.0, and the SR-alone constraint on  $\Delta w_a$  is reduced from 0.53 to 0.51).

#### 4.10 Utilizing CMB Constraints

We also computed the joint constraints on cosmological parameters from the scaling relations, number counts and from the CMB temperature and polarization anisotropy measurements by the upcoming *Planck* satellite. Table 10 presents these results. The *Planck* Fisher matrix is adopted from Heavens et al. (2007). This matrix assumes a flat universe, so we used the SR and NC matrices with the same assumption, and we placed a prior of 0.1 on all cluster parameters.

**Table 10.** Constraints including CMB anisotropy measurements by *Planck*. The constraints assume a flat universe, and a prior of 0.1 is applied to all cluster parameters. Only constraints on cosmological parameters are listed.

Parameter	SR	NC	Planck	Combined
$\Omega_m$	0.059	0.029	0.0023	0.0020
$\Omega_b$	0.015	0.012	0.00069	0.00059
$h$	0.080	0.11	0.0049	0.0042
$w_0$	0.14	0.20	0.35	0.04
$w_a$	0.33	0.52	1.26	0.12
$\sigma_8$	N/A	0.023	0.074	0.0050
$n_s$	N/A	0.26	0.0033	0.0022

Unsurprisingly, the addition of the SR+NC data improve little over the *Planck*-alone constraints for most cosmological parameters, except  $w_0$ ,  $w_a$  and  $\sigma_8$ . As is well known, the *Planck* data alone for these 3 parameters suffer from severe degeneracies (their degeneracy parameters  $\mathcal{D}$ , as defined in Table 1, are 161, 209 and 93 respectively). Adding the cluster data causes significant improvements in these parameters. In fact, the improvements in the SR+NC+*Planck* combination are significant compared either to SR+NC or to *Planck* alone; this shows that the improvements arise by breaking degeneracy between the *Planck* and cluster dataset. The joint constraints on  $w_0$  and  $w_a$  improve to the interestingly tight levels of 0.04 and 0.12, respectively.

#### 4.11 Covariance Between Scaling Relations and Number Counts

In our analysis, we have neglected correlations between the constraints derived from different observables, i.e., the Fisher matrices were simply added to obtain the joint constraints. Apart from possible systematic measurement errors, the  $Y$  vs.  $T$  measurements of two different clusters, in different regions of the sky, should indeed be uncorrelated (except, perhaps in the rare cases of very close neighbors physically affecting each other). On the other hand, it is not obvious whether correlations between the SR and NC approaches are negligible. For a given cluster, the  $Y - M$  and the  $Y - T$  relations could well be correlated, through the underlying physical origin of the scatter in these two relations. Those clusters with unusually high  $Y$  values would then also be more likely to be included in the detected sample. Indeed, in the limit that  $M$  and  $T$  are uniquely related without any scatter, deviations in  $Y$  from the expected  $\langle Y \rangle$  will change the  $Y-T$  relation and can simultaneously affect the number counts (by moving a cluster to a different  $Y$ -bin).

To see if this indeed introduces a significant correlation between the SR and NC constraints, we performed a suite of Monte Carlo calculations, in which 500,000 random realizations of a mock cluster catalog were generated. At the assumed redshift  $z = 0.5$ , each mock catalog contains  $\sim 2500$  clusters, drawn randomly from the underlying mass function above the mass limit of  $10^{14} M_\odot$ . This limit corresponds to an SZ signal of  $1\sigma$  at  $z = 0.5$ , sufficiently below the  $5\sigma$  detection threshold that clusters with masses below this limit have negligible chance to scatter above the detection threshold. The total number of clusters in each realization

of the mock catalog is drawn from a Poisson distribution with a mean of 2,500. The number of detected clusters is then  $\sim 400$ , which is roughly the number of clusters in the redshift bin  $0.45 < z < 0.5$  in our fiducial model, assuming the survey parameters given in § 2.5.

Using our cluster model, we assign a temperature and a  $Y$  parameter to each cluster, based on its mass. A 10% intrinsic scatter and a  $1\sigma$  measurement uncertainty, which are drawn independently from Gaussian distributions, are also added to the  $Y$  parameter, but no scatter is added to the temperature. By assigning scatter only to the  $Y$  parameter (and not to  $T$ ), the  $Y - M$  and  $Y - T$  relations are fully correlated, so that any resulting correlation between the SR and NC constraints will be overestimated. Maximum correlation between the two approaches is achieved by anti-correlating  $Y - M$  and  $Y - T$  relations, however, such anti-correlation does not seem physically realistic. We have assigned a Fisher matrix to each single cluster in the SR approach, and these Fisher matrices might have different correlation strength to the NC approach. For example, scaling relation Fisher matrix of a cluster with  $Y$  just above the detection threshold seems more correlated to NC approach than average, because scatter of  $Y$  can easily make it undetected and therefore change the number of detected clusters. So to be exact, we need consider correlation for each single SR Fisher matrix, which is a daunting task. Instead, In order to reduce the dimensions of the covariance matrix, we binned the SR observables into the same  $Y$  bins used for the number counts (this does not significantly change the SC constraints since the  $Y - T$  relation does not have small-scale features that would be missed by this binning). We then studied the correlation between cluster number  $N$  and the binned SR observable  $\bar{S} \equiv \langle Y/Y_0(T) \rangle_{\text{bin}}$ , where  $Y_0(T)$  is the  $Y$  parameter computed from the cluster model (without scatter), and the subscript “bin” indicates that the averaging is over all clusters in a  $Y$  bin (as opposed to over Monte Carlo realizations).

As a result of the intrinsic scatter and the measurement uncertainty,  $\bar{S}$  generally deviates from unity. Using the 500,000 Monte Carlo realizations, we computed the following three types of correlation coefficients:

$$r_{N_i N_j} = \frac{\text{Cov}(N_i, N_j)}{\sigma_{N_i} \sigma_{N_j}},$$

$$r_{N_i \bar{S}_j} = \frac{\text{Cov}(N_i, \bar{S}_j)}{\sigma_{N_i} \sigma_{\bar{S}_j}},$$

$$r_{\bar{S}_i \bar{S}_j} = \frac{\text{Cov}(\bar{S}_i, \bar{S}_j)}{\sigma_{\bar{S}_i} \sigma_{\bar{S}_j}},$$

where  $i$  and  $j$  refer to the  $Y$ -bin indices and, e.g.,  $\text{Cov}(N_i, N_j) \equiv \langle (N_i - \bar{N}_i)(N_j - \bar{N}_j) \rangle^{1/2}$ , where bar denotes averaging within the  $Y$ -bin, and the other correlation coefficients are defined similarly. First, without any scatter on  $Y$ , we checked that no correlation is introduced artificially in the treatment outlined above (i.e. all coefficients  $r$  are zero). When we include the scatter on  $Y$ , we find all three types of correlations coefficient are a few  $\times 10^{-3}$ , which is still consistent with zero within the uncertainty of the calculation.

While this result may be surprising, the lack of correlations is explained by the fact that the  $Y$ -values are still drawn independently for each cluster, even after the scatter is included. In particular, moving clusters across adjacent

$Y$ -bins clearly introduces correlations in the number of excess clusters *relative to the no-scatter case*. The inclusion of scatter, however, also changes the mean number of clusters in each  $Y$ -bin, and the  $Y/T$  ratio in these bins. It is the excursions around these modified mean values that we find to be essentially uncorrelated. In the Appendix, we use a simplified toy model, in which we show that the covariance between neighboring bins  $\text{Cov}(N_i, N_j)$  is strictly zero; one can similarly show  $\text{Cov}(N_i, \bar{S}_j) = 0$  and  $\text{Cov}(\bar{S}_i, \bar{S}_j) = 0$ .

#### 4.12 The Importance of the Virial Overdensity

Finally, as mentioned above, there is an apparent tension between our results, and the conclusions reached recently by Aghanim et al. (2008), who find that the scaling relations are little affected by changes in the dark-energy equation of state. However, we believe these two results are not, in fact, in contradiction. We find that the dark energy parameters  $w_0$  and  $w_a$  indeed have only a small direct effect on the scaling relation. For instance, we find that the value of  $Y$  for a cluster with a fixed temperature, at  $z = 0.2$ , increases by about 4% when changing  $w_0 = -1$  to  $w_0 = -1.2$  (see Table 2). This is consistent with Figure 4 in Aghanim et al., which shows that the normalization of the  $Y - T$  relation changes by a few percent over the  $-1.2 < w_0 < -0.8$  range, with the largest increase for the smallest value  $w_0 = -1.2$  consistent with 4%. We note that Aghanim et al. also include a cosmology-dependent factor, which is a power-law in the normalized Hubble parameter  $E(z)$ , in their definition of  $Y$ . At low redshift, this factor is  $\sim 1$ , and does not drive the  $w_0$ -sensitivity. At higher redshifts, this factor drives the  $w_0$ -sensitivity; if we were to scale out this factor from the definition of  $Y$ , at  $z = 1.5$  we would predict a  $\sim 3\%$  increase in  $Y$  when changing  $w_0 = -1$  to  $w_0 = -1.2$  which is again consistent with the change seen in Figure 4 in Aghanim et al. (their middle panel). The constraints we obtain here on  $w_0$  and  $w_a$  derive in large part from this modest dependence of the scaling relations on the dark energy equation of state, and owe much to the large number of clusters and relatively weak degeneracies. Our results are also explicitly based on the simulations by Kuhlen et al. (2005) on how dark energy affect the virial overdensity. Although there is no clear sign of any disagreement, it would be worthwhile to explicitly check the consistency between the  $w_0$ -dependence of the virial overdensity between the two simulations.

## 5 CONCLUSIONS

In this paper, we studied the utility of the scaling relation between the Sunyaev-Zeldovich decrement  $Y$  and temperature  $T$  of galaxy clusters; in particular, the constraint that this relation may place on cosmological and on cluster structural parameters. A phenomenological cluster model is adopted, which has 15 free parameters to describe cluster structure, and its dependence on mass and redshift. We demonstrated that this model fits available cluster observations, including the temperature profile outside the core. We then used this model to forecast constraints that could become available from a future survey, containing several thousand clusters.

Our basic result is that the scaling relations have a statistical constraining power on cosmological parameters com-

parable to those from cluster number counts, even after we marginalize over the cluster parameter uncertainties. We investigated where the cosmology sensitivity in the scaling relation comes from, and found that the constraints are driven by different physics for different parameters. The constraints on  $\Omega_m$  and  $\Omega_b$  arise mainly through the gas fraction  $f_g$ ; the constraints on  $\Omega_{DE}$  and  $h$  are predominantly through  $D_A$ , and the constraints on  $w_0$  and  $w_a$  are driven by the characteristic virial overdensity  $\Delta_{\text{vir}}$  at low redshifts, but by  $D_A$  at high redshifts.

The scaling relation constraints have significant degeneracies. The most significant of these is between  $\Omega_b$  and  $\Omega_m$ , whereas the parameters suffering the least degeneracy are  $w_0$  and  $w_a$ . These dark energy equation-of-state parameters have statistical errors from the scaling relations that are somewhat tighter than from the number counts. Combining the scaling relation with the number counts, including multiple  $Y$ -bins, and combining cluster data with expected CMB temperature and polarization measurements by *Planck* all help in breaking parameter degeneracies. In a model that uses 6,800 clusters, and combines the SR+NC+*Planck* data, and assumes a prior of 10% on the 15 cluster model parameters, we find tight constraints on the dark energy equation of state parameters,  $\Delta w_0 = 0.04$  and  $\Delta w_a = 0.12$ .

The most significant caveat to our conclusions is that we assumed a particular parameterization of the cluster model. Strictly speaking, our numerical results are valid only within the confines of this specific model. However, our results do indicate, more generally, that there will be significant statistical constraining power in the scaling relations data, and that there is also sufficient cosmological sensitivity in the scaling relations to be relevant as a cosmology probe. The latter point is the main new conclusion of this work. Indeed, the cosmology-dependencies that we find drives the SR constraints should be relatively robust features:  $D_A$ ,  $\Delta_{\text{vir}}$ , and  $f_g$  are likely to depend on cosmology, in any reasonable cluster model, in the way we exploited here. Indeed, the likely outcome of the analysis of any actual cluster survey data is that it will force us to adopt some other, physically motivated parametric description of cluster structure, and the parameters of that new model will then have to be constrained, together with the cosmological parameters.

We have studied various other explicit caveats, such as the impact of partial X-ray coverage of the SZ sample, or uncertain scatter and completeness, or departures from simple power-laws in the dependence of the cluster parameters on mass and redshift. We generally find that the constraints loosen, as expected, but remain appreciable. Overall, our work suggests that explicit scaling relations do not, by themselves, strongly constrain the highly degenerate cluster parameters, but that they should be a useful component in extracting cosmological information from large future cluster surveys.

## ACKNOWLEDGMENTS

We thank Wenjuan Fang, Sheng Wang, Neelima Sehgal, Gil Holder, Amber Miller, and Greg Bryan for many useful discussions, and the anonymous referee for useful comments. ZH acknowledges support by the Polányi Program of the Hungarian National Office of Technology and by

the NSF grant AST-05-07161. LV acknowledges the support of Marie Curie International Reintegration Grant FP7-PEOPLE-2007-4-3-IRGn202182.

## REFERENCES

- Abbott, T. et al. 2005, astro-ph/0510346
- Afshordi, N. 2008, ApJ, 686, 201
- Aghanim, N., da Silva, A. C., & Nunes, N. J. 2008, arXiv:0808.0385
- Allen, S. W., Rapetti, D. A., Schmidt, R. W., Ebeling, H., Morris, R. G. & Fabian, A. C. 2008, MNRAS, 383, 879
- Albrecht, A. et al. 2006, “Report of the Dark Energy Task Force”, preprint astro-ph/0609591
- Ascasibar, Y., & Diego, J. M. 2008, MNRAS, 383, 369
- Birkinshaw M., 1999, Phys. Rep., 310, 97
- Blake, C., & Glazebrook, K. 2003, ApJ, 594, 665
- Bonamente, M., Joy, M. K., LaRoque, S. J., Carlstrom, J. E., Reese, E. D., & Dawson, K. S. 2006, ApJ, 647, 25
- Borgani, S., Governato, F., Wadsley, J., Menci, N., Tozzi, P., Lake, G., Quinn, T., & Stadel, J. 2001, ApJ, 559, 71
- Bryan, G. L., & Norman, M. L. 1998, ApJ, 495, 80
- Cavaliere, A., & Fusco-Femiano, R. 1976, A&A, 49, 137
- Carlstrom, J. E., Holder, G. P., & Reese, E. D. 2002, ARA&A, 40, 643
- Duffy, A. R., Schaye, J., Kay, S. T., & Dalla Vecchia, C. 2008, MNRAS, 390, L64
- Dunkley, J. et al. 2008, ApJS, in press, preprint arXiv:0803.0586
- Fang, W., & Haiman, Z. 2007, Phys. Rev. D, 75, 3010
- Fang, W., & Haiman, Z. 2008, ApJ, 680, 200
- Faltenbacher, A., Kravtsov, A. V., Nagai, D., & Gottlöber, S. 2005, MNRAS, 358, 139
- Fisher, R. A. 1935, J. Roy. Stat. Soc., 98, 39
- Haiman, Z., Mohr, J. J., & Holder, G. 2001, ApJ, 553, 545
- Haiman, Z. et al. 2005, “An X-ray Galaxy Cluster Survey for Investigations of Dark Energy”, White Paper submitted to the Dark Energy Task Force; available as preprint astro-ph/0507013
- Heavens, A. F., Kitching, T. D., Verde, L. 2007, MNRAS, 380, 1029
- Helsdon, S. F., & Ponman, T. J. 2000, MNRAS, 315, 356
- Henry, J. P. 2000, ApJ, 534, 565
- Henry, J. P. 2004, ApJ, 609, 603
- Holder, G. P., Haiman, Z., & Mohr, J. J. 2001, ApJ, 560, L111
- Hu, W. 2003, Phys. Rev. D, 67, 081304
- Hu, W., & Haiman, Z. 2003, Phys. Rev. D, 68, 3004
- Hu, W., & Kravtsov, A. V. 2003, ApJ, 584, 702
- Ikebe, Y., Reiprich, T. H., Böhringer, H., Tanaka, Y., & Kitayama, T. 2002, A&A, 383, 773
- Jenkins, A., Frenk, C. S., White, S. D. M., Colberg, J. M., Cole, S., Evrard, A. E., Couchman, H. M. P., & Yoshida, N. 2001, MNRAS, 321, 372
- Kaiser, N., 1986, MNRAS, 222, 323
- Kay, S. T., Thomas, P. A., Jenkins, A., & Pearce, F. R. 2004, MNRAS, 355, 1091
- Kirkman, D., Tytler, D., Suzuki, N., O’Meara, J. M., & Lubin, D. 2003, ApJS, 149, 1
- Komatsu, E., & Seljak, U. 2001, MNRAS, 327, 1353
- Komatsu, E., et al. 2009, ApJS, 180, 330
- Kosowsky, A., Milosavljevic, M., Jimenez, R. 2002, PRD, 66, 3007
- Kravtsov, A. V., Vikhlinin, A., & Nagai, D. 2006, ApJ, 650, 128
- Kuhlen, M., Strigari, L. E., Zentner, A. R., Bullock, J. S., & Primack, J. R. 2005, MNRAS, 357, 387
- Leccardi, A., & Molendi, S. 2008, A&A 486, 359
- Lima, M., & Hu, W. 2004, Phys. Rev. D, 70, 043504
- Lima, M., & Hu, W. 2005, Phys. Rev. D., 72, 043006
- Linder, E. V. 2003, Phys. Rev. D., 68, 3504
- Majumdar, S., & Mohr, J. J. 2003, ApJ, 585, 603
- Majumdar, S., & Mohr, J. J. 2004, ApJ, 613, 41
- Mantz, A., Allen, S. W., Ebeling, H., & Rapetti, D. 2008, MNRAS, 387, 1179
- Molnar, S. M., Hearn, N., Haiman, Z., Bryan, G. L., Evrard, A. E., & Lake, G. 2008, ApJ, submitted
- Morandi, A., Ettori, S., & Moscardini, L. 2007, MNRAS, 379, 518
- Mroczkowski, T. et al. 2008, ApJ, submitted, preprint arxiv.org:0809.5077
- Nagai, D. 2006, ApJ, 650, 538
- Navarro, J. F., Frenk, C. S., & White, S. D. M. 1997, ApJ, 490, 493 (NFW)
- Ostriker, J. P., Bode, P., & Babul, A. 2005, ApJ, 634, 964
- Ponman, T. J., Sanderson, A. J. R., & Finoguenov, A. 2003, MNRAS, 343, 331
- Pratt, G. W., Arnaud, M., & Pointecouteau, E. 2006, A&A, 446, 429
- Rasia, E., Tormen, G., & Moscardini, L. 2004, MNRAS, 351, 237
- Raymond, J. C. & Smith, B. W. 1977, ApJS, 35, 419
- Reid, B. A., & Spergel, D. N. 2006, ApJ, 651, 643
- Reiprich, T. H., & Böhringer, H. 2002, ApJ, 567, 716
- Refregier, A., Valtchanov, I., & Pierre, M. 2002, A&A, 390, 1
- Sehgal, N., Trac, H., Huffenberger, K., & Bode, P. 2007 ApJ, 664, 149
- Seo, H.-J., & Eisenstein, D. J. 2003, ApJ, 598, 720
- Spergel, D. N. et al. 2007, ApJS, 170, 377
- Sunyaev, R. A., & Zeldovich, Ya. B. 1972, CoASP, 4, 173
- Tegmark, M., Taylor, A. N., & Heavens, A. F. 1997, ApJ, 480, 22
- Tozzi, P., & Norman, C. 2001, ApJ, 546, 33
- Verde, L., Haiman, Z., & Spergel, D. N. 2002, ApJ, 581, 5 (VHS02)
- Vikhlinin, A., Kravtsov, A., Forman, W., Jones, C., Markevitch, M., Murray, S. S., & Van Speybroeck, L. 2006, ApJ, 640, 691
- Vikhlinin, A. et al. 2008, ApJ, submitted, preprint arXiv:0805.2207
- Voit, G. M. 2005, Rev. Mod. Phys., 77, 207
- Voit, M., Bryan, G. L., Balogh, M. L., & Bower, R. G. 2002, ApJ, 576, 601
- Voit, G. M., Balogh, M. L., Bower, R. G., Lacey, C. G., & Bryan, G. L. 2003, ApJ, 593, 272
- Wang, S., Khoury, J., Haiman, Z., May, M. 2004, Phys. Rev. D., 70, 7013008
- Wechsler, R.H., Bullock, J.S., Primack, J. R., Kravtsov A. V., & Dekel, A. 2002, ApJ, 568, 52
- Younger, J. D., & Bryan, G. L. 2007, ApJ, 666, 647
- Younger, J. D., Haiman, Z., Bryan, G. L., & Wang, S. 2006, ApJ, 653, 27

Zhang, Y. Y., Finoguenov, A., Böhringer, H., Kneib, J. P., Smith, G. P., Kneissl, R., Okabe, N., & Dahle, H. 2008, *A&A*, 482, 451

## APPENDIX A: SCATTER AND THE (LACK OF) CORRELATIONS

As mentioned in § 4.11 in the text, in the limit that  $M$  and  $T$  are uniquely related without any scatter, deviations in  $Y$  around its mean value ( $\bar{Y}$ ) can simultaneously change the  $Y$ - $T$  relation and affect the number counts (by moving a cluster to a different  $Y$ -bin). It is not a-priori obvious whether this introduces correlations between the number counts in different  $Y$  bins, and/or cross-correlations between the scaling relations and the number counts. However, in § 4.11, we performed Monte Carlo simulations and found that that the correlations and cross-correlations are both negligibly small. In this Appendix, we illustrate how this (lack of) correlation can arise, using a simplified toy model.

Consider an experiment in which there are two bins, initially with a random number  $n_1$  and  $n_2$  of objects in each bin, drawn independently from Poisson distributions with means of  $\bar{n}_1$  and  $\bar{n}_2$ . Subsequently, each object in bin #1 is either relocated to bin #2 with a probability  $p$ , or left in bin #1, with a probability of  $(1-p)$ , after which there are  $N_1$  and  $N_2$  objects in the two bins. To simplify the mathematics below, we do not consider relocating objects from bin #2 to bin #1; this does not affect the essence of the argument. The covariance between  $N_1$  and  $N_2$  can be written as

$$\begin{aligned} \text{Cov}(N_1, N_2) &= \text{Cov}(N_1, N_2 - n_2 + n_2) \\ &= \text{Cov}(N_1, \Delta n + n_2) \\ &= \text{Cov}(N_1, \Delta n) + \text{Cov}(N_1, n_2), \\ &= \text{Cov}(N_1, \Delta n) + \text{Cov}(n_1 - \Delta n, n_2), \\ &= \text{Cov}(N_1, \Delta n) - \text{Cov}(\Delta n, n_2), \end{aligned} \quad (\text{A1})$$

where  $\Delta n \equiv N_2 - n_2 = n_1 - N_1$  is the number of objects relocated from bin #1 to bin #2, and in the last step, we have used  $\text{Cov}(n_1, n_2) = 0$ , which is true by construction.

In order to compute the last two terms on the right hand side, we first need to know the probability distribution of  $\Delta n$ ,

$$P(\Delta n) = \sum_{n_1=\Delta n}^{\infty} P(\Delta n|n_1)P(n_1). \quad (\text{A2})$$

By definition,  $n_1$  is drawn from Poisson distribution,

$$P(n_1) = \text{Pois}(n_1; \bar{n}_1) = \frac{\bar{n}_1^{n_1} e^{-\bar{n}_1}}{n_1!}, \quad (\text{A3})$$

and, given  $n_1$ ,  $\Delta n$  follows a binomial distribution,

$$\begin{aligned} P(\Delta n|n_1) &= \text{Bino}(\Delta n; n_1, p) \\ &= \frac{n_1!}{\Delta n!(n_1 - \Delta n)!} p^{\Delta n} (1-p)^{n_1 - \Delta n}. \end{aligned} \quad (\text{A4})$$

Substituting equations A3 and A4 to equation A2, we find

$$\begin{aligned} P(\Delta n) &= \quad (\text{A5}) \\ &= \sum_{n_1=\Delta n}^{\infty} \frac{\bar{n}_1^{n_1} e^{-\bar{n}_1}}{n_1!} \frac{n_1!}{\Delta n!(n_1 - \Delta n)!} p^{\Delta n} (1-p)^{n_1 - \Delta n} \\ &= \sum_{n_1=\Delta n}^{\infty} \frac{\bar{n}_1^{n_1} e^{-\bar{n}_1}}{\Delta n!(n_1 - \Delta n)!} p^{\Delta n} (1-p)^{n_1 - \Delta n}. \end{aligned}$$

Substituting  $n_1 = N_1 + \Delta n$ , and moving outside the summation all factors not containing  $N_1$ , equation A5 is simplified to

$$P(\Delta n) = \frac{e^{\bar{n}_1} (\bar{n}_1 p)^{\Delta n}}{\Delta n!} \sum_{N=0}^{\infty} \frac{(\bar{n}_1 (1-p))^{N_1}}{N_1!}. \quad (\text{A6})$$

Equation A6 can be simplified further by noting that the summation on the right hand side is the Taylor expansion of  $e^{\bar{n}_1 (1-p)}$ . After this simplification, we obtain the final expression of  $P(\Delta n)$ ,

$$P(\Delta n) = \frac{(p\bar{n}_1)^{\Delta n} e^{-p\bar{n}_1}}{\Delta n!} = \text{Pois}(\Delta n; p\bar{n}_1). \quad (\text{A7})$$

This corresponds to the intuitive result that  $\Delta n$  follows a Poisson distribution with a mean of  $p\bar{n}_1$ . It can be shown similarly that  $P(N_1) = \text{Pois}(N_1; (1-p)\bar{n}_1)$  and  $P(N_2) = \text{Pois}(N_2; \bar{n}_2 + p\bar{n}_1)$ .  $\text{Cov}(N_1, \Delta n)$  can now be computed by considering the variance of  $n_1$ ,

$$\begin{aligned} \text{Var}(n_1) &= \text{Var}(N_1 + \Delta n) \\ &= \text{Var}(N_1) + \text{Var}(\Delta n) + 2\text{Cov}(N_1, \Delta n). \end{aligned} \quad (\text{A8})$$

Since  $n_1$ ,  $N_1$  and  $\Delta n$  all follow Poisson distributions, their variances are equal to their expectation values, which are  $\bar{n}_1$ ,  $(1-p)\bar{n}_1$  and  $p\bar{n}_1$ , respectively. With this information, it follows from equations A2 and A10 that

$$\text{Cov}(N_1, \Delta n) = 0. \quad (\text{A9})$$

Similarly,  $\text{Cov}(\Delta n, n_2) = 0$  follows by considering the variance

$$\begin{aligned} \text{Var}(N_2) &= \text{Var}(n_2 + \Delta n) \\ &= \text{Var}(n_2) + \text{Var}(\Delta n) + 2\text{Cov}(\Delta n, n_2), \end{aligned} \quad (\text{A10})$$

and noting  $\text{Var}(N_2) = \bar{n}_2 + p\bar{n}_1$ ,  $\text{Var}(n_2) = \bar{n}_2$ , and  $\text{Var}(\Delta n) = p\bar{n}_1$ . This concludes the proof that  $\text{Cov}(N_1, N_2) = \text{Cov}(N_1, \Delta n) + \text{Cov}(\Delta n, n_2) = 0$ .

The derivation above can be generalized to show  $\text{Cov}(N_i, N_j) = 0$  when  $i \neq j$  in the case of multiple  $Y$  bins. Similar to equation A1,  $\text{Cov}(N_i, N_j)$  could be decomposed as

$$\begin{aligned} \text{Cov}(N_i, N_j) &= \text{Cov}\left(\sum_l \Delta n_{l \rightarrow i}, \sum_m \Delta n_{m \rightarrow j}\right) \\ &= \sum_{l,m} \text{Cov}(\Delta n_{l \rightarrow i}, \Delta n_{m \rightarrow j}), \end{aligned} \quad (\text{A11})$$

where  $n_{l \rightarrow i}$  is the number of clusters relocated from bin # $l$  to bin # $i$  by the scatter. For  $l \neq m$ ,  $\text{Cov}(\Delta n_{l \rightarrow i}, \Delta n_{m \rightarrow j}) = 0$  because of the independence between  $n_l$  and  $n_m$ , the number counts in the absence of scatter. To compute  $\text{Cov}(\Delta n_{l \rightarrow i}, \Delta n_{l \rightarrow j})$ , we first need the probability distributions of  $\Delta n_{l \rightarrow i}$ ,  $\Delta n_{l \rightarrow j}$  and  $\Delta n_{l \rightarrow i, j} \equiv (\Delta n_{l \rightarrow i} + \Delta n_{l \rightarrow j})$ . Following a procedure similar to the case of two bins above, we can show that these quantities all follow Poisson distributions with expectation values of  $p_{l \rightarrow i} \bar{n}_l$ ,  $p_{l \rightarrow j} \bar{n}_l$  and

$p_{l \rightarrow i, j} = (p_{l \rightarrow i} + p_{l \rightarrow j})\bar{n}_l$ , respectively. Here,  $p_{l \rightarrow i}$  is the probability of a cluster in bin # $l$  being scattered into bin # $i$ . For the Gaussian scatter assumed in this paper,

$$p_{l \rightarrow i} = \frac{\int_{M_{\min}(Y_i)}^{M_{\max}(Y_i)} g(Y_i, M) \frac{dn}{dM} dM}{\int_{M_{\min}(Y_l)}^{M_{\max}(Y_l)} \frac{dn}{dM} dM}, \quad (\text{A12})$$

where  $M_{\min}(Y_l)$  and  $M_{\max}(Y_l)$  are the minimum and maximum masses in bin # $l$  in the absence of scatter, and  $g(Y_i, M)$  was given in equation (21). By considering  $\text{Var}(\Delta n_{l \rightarrow i, j})$ , one can then show  $\text{Cov}(\Delta n_{l \rightarrow i}, \Delta n_{l \rightarrow j}) = 0$ ; substituting back into equation (A11), we find  $\text{Cov}(N_i, N_j) = 0$ .